AIAA JOURNAL
Vol. 46, No. 12, December 2008

Computations of Homogeneous-Equilibrium Two-Phase Flows with Accurate and Efficient Shock-Stable Schemes

Seung-Won Ihm* and Chongam Kim†
Seoul National University, Seoul 151-742, Republic of Korea

DOI: 10.2514/1.35097

For accurate and efficient computations of compressible gas–liquid two-phase mixture flows, the AUSMPW+ and RoeM schemes (for which the accuracy, efficiency, and robustness have been successfully demonstrated in gas dynamics) are extended to two-phase flows at all speeds. From the mixture equations of state, a new shock-discontinuity-sensing term suitably scaled for two-phase flows is derived and its performance is validated. In addition, several numerical difficulties appearing in the development of the two-phase AUSMPW+ and RoeM schemes are analyzed and successfully cured. The two-phase AUSMPW+ and RoeM schemes are then efficiently preconditioned for the simulation of all Mach number flows by employing the existing AUSM or Harten–Lax–van Leer with contact restoration types of preconditioning strategies. Various gas–liquid two-phase flows, from highly compressible to nearly incompressible flow conditions, are tested. The numerical results show the accurate and robust behavior of the proposed schemes for all speeds of two-phase flows.

Nomenclature

Cp_i	=	specific heat for the ith phasic fluid
c	=	speed of sound
E, F	=	inviscid flux vectors in the ξ and η directions
E_t	=	specific total internal energy $[e + (u^2 + v^2)/2]$
e	=	specific internal energy
H	=	specific total enthalpy $[h + (u^2 + v^2)/2]$
h	=	specific enthalpy $(e + p/\rho)$
M	=	Mach number
Q	=	vector of conservative variables $([\rho_m, \rho_m u, \rho_m v, \rho_m E_t, \rho_m Y_1]^T)$
T	=	temperature
t	=	time
u, v	=	Cartesian velocities in the x and y directions
V	=	local velocity magnitude $[(u^2 + v^2)^{1/2}]$
x, y	=	Cartesian coordinates
Y	=	mass fraction
α	=	volume fraction
β	=	pseudocompressibility parameter
ξ, η	=	generalized curvilinear coordinates
ρ	=	density

Subscripts

i	=	ith phasic quantity (1 for the gas phase and 2 for the liquid phase)
L, R	=	left and right quantities across a cell interface
m	=	two-phase mixture quantity
$1/2$	=	quantity at a cell interface
∞	=	freestream quantity

Presented as Paper 4457 at the 18th AIAA Computational Fluid Dynamics Conference, Miami, FL, 25–28 June 2007; received 12 October 2007; revision received 7 August 2008; accepted for publication 12 August 2008.

*Ph.D. Candidate, Department of Aerospace Engineering.
†Associate Professor, Department of Aerospace Engineering, Institute of Advanced Aerospace Technology; chongam@snu.ac.kr. Senior Member AIAA (Corresponding Author).

I. Introduction

RECENTLY, there have been numerous studies on the computation of compressible gas–liquid two-phase flows, because of its wide applications such as cavitation phenomena in hydraulic machines, high-speed underwater projectiles, explosions in water, liquid-shock/gas-bubble interaction, and so on. The popular mathematical modeling for the two-phase-flow physics can be largely classified into two approaches: two-fluid model and homogeneous-equilibrium model.

In the two-fluid model, two sets of conservation laws for each phase are directly solved. The two-fluid model can describe physical interactions at phase interface in detail but is known to suffer from a nonhyperbolic property, which causes numerical difficulties. Though there has been continuous research in this area [1,2], the remedy does not seem to be settled completely yet. Another drawback of the two-fluid model is the rapid increase of computational cost, especially when phase interface and shock wave coexist.

In the homogeneous-equilibrium model (HEM), the dynamic and thermal equilibriums of both phases are assumed within the same computational mesh, and only the momentum- and energy-conservation laws for the mixture is considered, along with the mass-conservation law for each phase (sometimes a single continuity equation is used and phase is determined from the equation of state). Though this approach has a limitation in capturing detailed interphasic flow physics, there have been plenty of computational studies using the HEM ([3–6], for example), due to its computational efficiency and conservative form.

The goal of the present work is to design and validate accurate and efficient numerical fluxes for the simulation of compressible two-phase flows under the homogeneous-equilibrium assumption. To realize this goal, a numerical scheme should satisfy several conditions.

First, a numerical scheme must be able to handle shock wave and phase interface robustly. Regarding the two-phase equation of state (EOS), it is found that a simple approximation of the mixture EOS fails near a phase interface [7], but the mixture EOS defined by the volumetric average of each phase's EOS does not trigger numerical instability [8]. Actually, there has been much research using the mixture EOS. For example, Kunz et al. [3] solved various two-phase flows, including three-dimensional unsteady supercavitating flows, sheet cavitation in turbomachinery, and axisymmetric underwater propulsion. Owis and Nayfeh [4] also analyzed cavitation flows around high-speed underwater vehicles. The work of Neaves and Edwards [6] includes several two-phase shock-tube problems and a water-entry simulation of supercavitating projectiles. According to

the authors' knowledge, however, the instability of a numerical flux caused by shock wave in two-phase mixture flows does not seem to be clearly analyzed yet. In compressible two-phase mixture flows, the stable and accurate treatment of shock waves is crucial in determining the overall quality of computed solutions. Thus, the consistent extension of shock-stable schemes demonstrated in single-phase gas dynamics to two-phase mixture flows is a subject worthy of careful study. In addition, a numerical scheme should be able to cover not only common mixture flows, but also phase-interfacial problems accompanying a large discrepancy of flow properties. For example, there are many air–water compressible two-phase flows such as compressible bubbly flow, free surface, compressible bubble rising, and so forth. A numerical scheme should be able to handle complex flow situations involving phase interface, shock waves, and their interactions.

Second, a numerical scheme must be able to cover a wide range of two-phase-flow regimes. The speed of sound in the liquid phase is about 1400–1500 m/s and it reduces to about 300–400 m/s in the gas phase. In the mixture region, it can be even lower. Because of the large variation in the speed of sound, compressible and incompressible regions coexist for many gas–liquid two-phase problems. From the viewpoint of the compressible governing equations, the condition number (the ratio of the largest to the smallest eigenvalue) becomes very large in the low-Mach-number region. As a result, the compressible governing equations face up to a stiffness problem that makes computed solutions difficult to converge. Thus, system preconditioning techniques have been developed and applied by several researchers [9,10]. Meanwhile, from the viewpoint of numerical dissipation, the solution accuracy of most upwind schemes cannot be guaranteed for the low-Mach-number region. This is because most upwind fluxes are designed to consider system eigenvalues, and thus the resultant numerical dissipation is scaled by the speed of sound, which becomes too large compared with local velocity in the low-Mach-number region. There have been studies on the construction of all-speed two-phase versions of AUSM-type [5] and Roe's flux-difference-splitting (FDS) [3] schemes using the preconditioned-system eigenvalues.

Keeping these in mind, the AUSMPW+ [11] and RoeM [12] schemes proposed by the authors are considered as two candidates for high-resolution compressible two-phase computations, for which the accuracy, efficiency, and robustness have been demonstrated in gas dynamics. The AUSMPW+ scheme is an improved version of the AUSMPW scheme [13]. With pressure-based weighting functions, AUSMPW+ can reflect both properties across a cell interface adequately. The numerical results of AUSMPW+ show the successful elimination of overshoots behind strong shocks and/or oscillations near a wall, which is a typical symptom appearing in most AUSM-type schemes. The RoeM scheme, based on Roe's FDS, shows the remarkably improved shock stability without any tunable parameters while maintaining the accuracy of the original Roe scheme. From the linear perturbation analysis of the odd–even decoupling problem, properly scaled Mach-number-based functions are introduced in RoeM to eliminate the shock instability of the original Roe scheme. The objective of the present work is the extension of the AUSMPW+ and RoeM schemes to compressible gas–liquid two-phase flows at all Mach numbers without compromising the merits of the original schemes in gas dynamics.

Both AUSMPW+ and RoeM schemes possess some shock-discontinuity-sensing terms (SDST) based on local pressure or Mach number distribution, which play a key role in determining their numerical performances. To keep the merits of both schemes in two-phase flows, we introduce a well-scaled SDST directly derived from the mixture EOS. In addition, numerical instabilities near a large-density-ratio phase interface, caused by the advection property of AUSM-type schemes, are cured by scaling the control functions of the AUSMPW+ scheme. Then we extend the two-phase version AUSMPW+ and RoeM to all Mach number flows by employing the preconditioning strategies of Edwards and Liou [14] and Luo et al. [15].

This paper is organized as follows: After the Introduction, the two-phase governing equations with the EOS for each phase are explained in Sec. II. The two baseline schemes (i.e., the original AUSMPW+ and RoeM for perfect-gas flows) are briefly introduced in Sec. III. In Sec. IV, a new SDST for two-phase flow is then derived and its performance is evaluated. The two-phase version of the AUSMPW+ and RoeM schemes is then presented in Sec. V, with the preconditioning strategies discussed in Sec. VI. Numerical results and comparisons for various test problems and some application problems are provided in Sec. VII. Finally, the conclusions are given in Sec. VIII.

II. Governing Equations

The HEM with mass fraction is adopted to describe two-phase flows. Assuming fully compressible flows including thermal effect, the governing equations consist of mixture mass-, momentum-, and energy-conservation laws, together with a one-phase mass-conservation law. A system preconditioning is introduced to cover the low-Mach-number region. The preconditioned form of the two-dimensional Euler system can be written in ξ–η computational coordinates as follows:

$$\frac{\Gamma}{J}\frac{\partial Q_p}{\partial t}+\frac{\partial E}{\partial \xi}+\frac{\partial F}{\partial \eta}=0 \tag{1}$$

where J indicates the Jacobian matrix. The primitive variable vector Q_p and the ξ-directional inviscid flux vector E are defined by

$$Q_p=[p,u,v,h_m,Y_1]^T \tag{2}$$

$$E=[\rho_m U,\rho_m uU+n_x p,\rho_m vU+n_y p,\rho_m HU,\rho_m Y_1 U]^T \tag{3}$$

where p, ρ_m, h_m, and H are the pressure, mixture density, mixture enthalpy, and mixture total enthalpy, respectively; Y_1 stands for the mass fraction of the gas phase; $U=n_x u+n_y v$ is the contravariant velocity component normal to a control interface; and $n_x=\xi_x/J$ and $n_y=\xi_y/J$ are directional cosines. For viscous equations, the viscous term, along with suitable turbulence transport equations, is added as in single-phase flow. The mixture viscosity is computed based on volume fraction. For axisymmetric flows, extra flux source terms are simply added on the right-hand side.

The preconditioning matrix Γ has the following form:

$$\Gamma=\begin{pmatrix} \frac{1}{\beta} & 0 & 0 & \frac{\partial\rho_m}{\partial h_m} & \frac{\partial\rho_m}{\partial Y_1} \\ \frac{u}{\beta} & \rho_m & 0 & u\frac{\partial\rho_m}{\partial h_m} & u\frac{\partial\rho_m}{\partial Y_1} \\ \frac{v}{\beta} & 0 & \rho_m & v\frac{\partial\rho_m}{\partial h_m} & v\frac{\partial\rho_m}{\partial Y_1} \\ \frac{H}{\beta}-1 & \rho_m u & \rho_m v & \rho_m+H\frac{\partial\rho_m}{\partial h_m} & H\frac{\partial\rho_m}{\partial Y_1} \\ \frac{Y_1}{\beta} & 0 & 0 & Y_1\frac{\partial\rho_m}{\partial h_m} & \rho_m+Y_1\frac{\partial\rho_m}{\partial Y_1} \end{pmatrix} \tag{4}$$

In Eq. (4), the pseudocompressibility parameter β has a square value of the local velocity magnitude in a preconditioned form. If $1/\beta=\partial\rho_m/\partial p$, then Γ goes back to $\Gamma_e=\partial Q/\partial Q_p$, resulting in the nonpreconditioned system in the primitive form. The eigenvalues of the preconditioned Euler system are

$$\lambda\left(\Gamma^{-1}\frac{\partial E}{\partial Q_p}\right)=U,U,U,U'+D,U'-D \tag{5}$$

where

$$U'=\frac{1}{2}\left(1+\frac{c'^2}{c^2}\right)U \qquad D=\frac{1}{2}\sqrt{\left(1-\frac{c'^2}{c^2}\right)^2U^2+4c'^2}$$

$$\frac{1}{c'^2}=\frac{1}{\beta}+\frac{1}{\rho_m}\frac{\partial\rho_m}{\partial h_m}$$

The main purpose of the system preconditioning is to scale the system eigenvalues so that they have the same order of magnitude, which leads to convergence enhancement in the low-Mach-number region. Depending on the definition of the preconditioned sound speed c' or the pseudocompressibility parameter β, there are many variations [9,10], and the preconditioning technique of [16] is

adopted in the present work. The only modification is the smooth transition of the system eigenvalues from the order of the speed of sound to the order of the local velocity magnitude, $V = \sqrt{u^2 + v^2}$, in the region of $|M| \le 1/a_0$. As a result, the following definition of c' is used:

$$c'^2 = a_1 \times c^2 + (1 - a_1) \times \max(V^2, (0.1V_{\text{ref}})^2) \tag{6}$$

where

$$a_1 = \frac{1}{2}\left(\sin\left(\pi \times \min(1, a_0|M|) - \frac{\pi}{2}\right) + 1\right)$$

with $a_0 \ge 1$, where a_0 is a preconditioning parameter defined by users. For highly compressible two-phase flows, a large value of a_0 can be used, which changes the governing equations into the nonpreconditioned system. For all Mach number flow computations, the values of 1 to 10 are suggested. The continuous function a_1 is employed for the system eigenvalues to change smoothly in the range of $|M| \le 1/a_0$.

In the HEM, the definition of the mixture density ρ_m plays the role of the mixture EOS:

$$\rho_m = 1 \Big/ \sum_i \frac{Y_i}{\hat{\rho}_i(p, T)} = 1 \Big/ \sum_i \frac{Y_i}{\hat{\rho}_i(p, h_i)} \tag{7}$$

In Eq. (7), $\hat{\rho}_i$ is the density of the ith fluid on the occupied computational mesh, and ρ_m is the mixture density defined on the whole computational mesh.

For the gas phase, the ideal-gas EOS is used:

$$p = (\gamma - 1)\hat{\rho}_1 e_1 \tag{8}$$

where $\gamma = 1.4$. For the liquid phase, the following form of the stiffened EOS is adopted [17]:

$$p = (n - 1)\hat{\rho}_2 e_2 - n p_c \tag{9}$$

where $n = 7.0$ and $p_c = 3.03975 \times 10^8$ Pa. Unless otherwise stated, the density of gas and liquid at atmospheric conditions (p= 101325.0 Pa and $T = 288.49$ K) is $\rho_g = 1.225$ kg/m^3 and ρ_l= 1000.0 kg/m^3, respectively.

Finally, from the dynamic and thermal equilibrium within the same computational mesh, the total governing system is closed:

$$p = p_l = p_g \qquad T = T_l = T_g \tag{10}$$

The mixture enthalpy in Eq. (2) is defined as

$$h_m = \sum_i h_i Y_i \tag{11}$$

Assuming that both phases are calorically perfect, the following enthalpy-temperature relations are used:

$$h_i = Cp_i T - h_{0,i} \tag{12}$$

where $Cp_1 = 1003.5$ m^2/s^2 K and $h_{0,1} = 0.0$ m^2/s^2 for the gas phase, and $Cp_2 = 4180.0$ m^2/s^2 K and $h_{0,2} = 851133.67$ m^2/s^2 for the liquid phase, respectively.

III. Baseline Schemes: AUSMPW+ and RoeM for Compressible Gas Dynamics

Before deriving schemes for gas–liquid two-phase flows, we first introduce the baseline schemes for compressible gas flows. The AUSMPW+ and RoeM schemes are extended for two-phase flows at all Mach numbers. Both schemes are among the recently developed schemes for the efficient and accurate calculations of compressible gas flows, which especially focus on the enhanced shock stability without compromising the accuracy of the original schemes. Though it was shown in the very recent work of Kitamura et al. [18] that the well-known shock-capturing schemes, including AUSMPW+ and RoeM, are not carbuncle-free in a strict sense, the multidimensional dissipation employed in AUSMPW+ and RoeM is still effective for suppressing multidimensional carbuncle phenomena. In addition, the shock stability characteristics of AUSMPW+ and RoeM are relatively better and they exhibit more consistent numerical behavior than with other schemes (see [18] for further details).

A. AUSMPW+ Scheme

The numerical flux of AUSMPW+ [11] at a cell interface is written as follows:

$$E_{1/2} = \bar{M}_L^+ c_{1/2} Q_L^* + \bar{M}_R^- c_{1/2} Q_R^* + (P_L^+ P_L + P_R^- P_R) \tag{13}$$

For $M_{1/2} \ge 0$,

$$\bar{M}_L^+ = M_L^+ + M_R^-[(1 - \omega)(1 + f_R) - f_L]$$
$$\bar{M}_R^- = M_R^- \omega (1 + f_R)$$

For $M_{1/2} < 0$,

$$\bar{M}_L^+ = M_L^+ \omega (1 + f_L)$$
$$\bar{M}_R^- = M_R^- + M_L^+[(1 - \omega)(1 + f_L) - f_R]$$

where $Q^* = [\rho, \rho u, \rho v, \rho H]^T$ and $P = [0, n_x p, n_y p, 0]^T$ for two-dimensional gas flows. The Mach number is defined as $M = U/c_{1/2}$, and the numerical speed of sound is formulated as

$$c_{1/2} = \begin{cases} c_s^2 / \max(|U_L|, c_s), & U_L + U_R > 0 \\ c_s^2 / \max(|U_R|, c_s), & U_L + U_R < 0 \end{cases} \tag{14}$$

where

$$c_s = \sqrt{2(\gamma - 1)/(\gamma + 1) H_{\text{normal}}}$$

and

$$H_{\text{normal}} = 0.5 \times \left(H_L - 0.5 \times V_{t,L}^2 + H_R - 0.5 \times V_{t,R}^2\right)$$

where V_t indicates a tangential velocity component to a cell interface.

The Mach number interpolation functions in Eq. (13) are computed by the following van Leer splitting Mach number:

$$M^{\pm} = \begin{cases} \pm\frac{1}{4}(M \pm 1)^2 & |M| \le 1 \\ \frac{1}{2}(M \pm |M|) & |M| > 1 \end{cases} \tag{15}$$

$$P^{\pm} = \begin{cases} \frac{1}{4}(M \pm 1)^2 (2 \mp M) & |M| \le 1 \\ \frac{1}{2}(1 \pm \text{sign}(M)) & |M| > 1 \end{cases} \tag{16}$$

The pressure-based weighting functions ω and $f_{L,R}$ are designed by

$$\omega = 1 - \Pi_{1/2}^3 \tag{17}$$

and

$$f_{L,R} = \begin{cases} \left(\frac{p_{L,R}}{p_s} - 1\right) \times \min\left(1, \frac{\min(p_{L,1}, p_{R,1}, p_{L,2}, p_{R,2})}{\min(p_L, p_R)}\right)^2 & p_s \ne 0 \\ 0 & p_s = 0 \end{cases} \tag{18}$$

where

$$\Pi_{1/2} = \min\left(\frac{p_L}{p_R}, \frac{p_R}{p_L}\right)$$

and $p_s = P_L^+ p_L + P_R^- p_R$. Figure 1 shows the computational stencil for the functions ω and $f_{L,R}$. In the region of shock waves, AUSMPW+ considers Q_L^* and Q_R^* with the same order of magnitude via ω and $f_{L,R}$ to remove numerical oscillations of AUSM-type

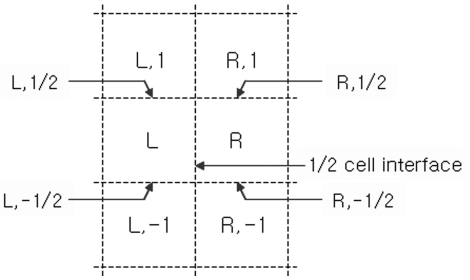

Fig. 1 Two-dimensional cell interface.

schemes. In addition, with $f_{L,R}$, AUSMPW+ has a dissipation term by pressure difference, thus pressure wiggles do not appear near the wall region. The detailed derivation and discussion of AUSMPW+ for gas dynamics can be found in [11].

B. RoeM Scheme

The RoeM scheme [12] for two-dimensional gas flows is summarized in a Harten–Lax–van Leer–Einfeldt (HLLE)-like form as

$$E_{1/2} = \tfrac{1}{2}[E_L + E_R - \tilde{M}A\Delta Q + \hat{c}(\tilde{M}^2 - 1)\Delta Q^* + g\hat{c}(1 - |\tilde{M}|)B\Delta Q^*] \tag{19}$$

$$B\Delta Q^* = \left(\Delta\rho - f\frac{\Delta p}{\hat{c}^2}\right)\begin{pmatrix}1\\ \hat{u}\\ \hat{v}\\ \hat{H}\end{pmatrix} + \hat{\rho}\begin{pmatrix}0\\ \Delta u - n_x\Delta U\\ \Delta v - n_y\Delta U\\ \Delta H\end{pmatrix} \tag{20}$$

where $\tilde{M} = \text{sign}(\hat{M}) \times \min(1, |\hat{M}|)$,

$$\hat{M} = \frac{\hat{U}}{\hat{c}} = \frac{n_x\hat{u} + n_y\hat{v}}{\hat{c}}$$

$Q = [\rho, \rho u, \rho v, \rho E_t]^T$ is the conservative variables vector, $A = \partial E/\partial Q$ is the system Jacobian matrix, and the properties with the hat symbol indicate Roe-averaged values. The Mach-number-based control functions f and g are defined as follows:

$$f = \begin{cases} 1 & \hat{u}^2 + \hat{v}^2 = 0 \\ |\hat{M}|^h & \hat{u}^2 + \hat{v}^2 \neq 0 \end{cases} \tag{21}$$

$$g = \begin{cases} |\hat{M}|^{1-\Pi_{1/2}} & \hat{M} \neq 0 \\ 1 & \hat{M} = 0 \end{cases} \tag{22}$$

where

$$h = 1 - \min(\Pi_{1/2}, \Pi_{L,1/2}, \Pi_{L,-1/2}, \Pi_{R,1/2}, \Pi_{R,-1/2})$$

The computational stencil for the functions f and g is presented in Fig. 1. Based on the stability analysis, the function f is designed to damp the feeding rate of pressure perturbation into density field, and the function g is designed to increase the damping rate of density perturbation and to control pressure perturbation simultaneously. As a result, the shock instability triggered by the pressure-difference term of the numerical mass flux is cured in the RoeM scheme.

By modifying the signal velocities to prevent expansion shock without compromising the capturing capability of contact discontinuity, the RoeM scheme is summarized as follows:

$$E_{1/2} = \frac{1}{b_1 - b_2}\left[b_1 \times E_L - b_2 \times E_R + b_1 \times b_2 \times \left(\Delta Q^* - \frac{g}{1 + |\tilde{M}|}B\Delta Q^*\right)\right] \tag{23}$$

where $b_1 = \max(\hat{U} + \hat{c}, U_R + \hat{c}, 0)$ and $b_2 = \min(\hat{U} - \hat{c}, U_L - \hat{c}, 0)$ (see [12] for further details).

IV. Shock-Discontinuity-Sensing for Two-Phase-Mixture Flows

The AUSMPW+ and RoeM schemes for gas dynamics have control functions that monitor pressure distribution around a cell interface. With this information, both schemes are able to sense shock discontinuity and control the amount of the numerical fluxes properly to enhance the stability and/or accuracy of the original AUSM-type or Roe-type schemes. A typical form of SDST included in the control functions of AUSMPW+ and RoeM schemes is to use the ratio of left to right pressure values across a cell interface:

$$\Pi_{1/2} = \min\left(\frac{p_L}{p_R}, \frac{p_R}{p_L}\right) \tag{24}$$

As can be seen in Eq. (24), $\Pi_{1/2}$ is designed to have a value of near 1 in the smooth region and near 0 in the discontinuous shock region. Inaccurate sensing of $\Pi_{1/2}$ eventually causes an improper amount of numerical dissipation in AUSMPW+ and RoeM, which yields a diffusive solution or numerical instabilities. Thus, a study on the pressure-field change must be carried out to design a relevant form of $\Pi_{1/2}$ for two-phase flows.

A. Pressure-Field Change in Two-Phase Flow

The starting point is that the pressure field usually varies with the order of dynamic pressure in smooth region. Thus, it is reasonable to assume the variation of pressure field to be in the range of

$$p_\infty \pm \frac{\rho_\infty u_\infty^2}{2}\mathcal{O}(1)$$

For the gas phase, the ideal-gas EOS [$p = (\gamma - 1)\rho e$] indicates

$$p_\infty = \frac{1}{\gamma}\rho_\infty c_\infty^2 = \frac{1}{\gamma M_\infty^2}\rho_\infty u_\infty^2 \tag{25}$$

From Eq. (25), $\frac{1}{2}\rho_\infty u_\infty^2 = \frac{\gamma}{2}M_\infty^2 p_\infty$, and thus

$$p_\infty \pm \frac{\rho_\infty u_\infty^2}{2}\mathcal{O}(1) = \left\{1 \pm \frac{\gamma M_\infty^2}{2}\mathcal{O}(1)\right\}p_\infty$$

If we have a sufficient number of grid points (say, N) in smooth subsonic flows changing from p_∞ to

$$p_\infty + \frac{\rho_\infty u_\infty^2}{2}\mathcal{O}(1)$$

then $\Pi_{k+1/2}$ of Eq. (24) at a cell interface $k + 1/2$ becomes

$$\Pi_{k+1/2} \approx \frac{p_\infty\left\{1 + \frac{\gamma M_\infty^2}{2}\mathcal{O}(1) \times \frac{k}{N}\right\}}{p_\infty\left\{1 + \frac{\gamma M_\infty^2}{2}\mathcal{O}(1) \times \frac{k+1}{N}\right\}} = \frac{1 + \frac{\gamma M_\infty^2}{2}\mathcal{O}(1) \times \frac{k}{N}}{1 + \frac{\gamma M_\infty^2}{2}\mathcal{O}(1) \times (\frac{k}{N} + \frac{1}{N})} \tag{26}$$

Because

$$N \gg \frac{\gamma M_\infty^2}{2}\mathcal{O}(1)$$

$\Pi_{k+1/2}$ is close to unit and it correctly senses the smooth region.

For the liquid phase, the stiffened-fluid EOS [$p = (n - 1)\rho e - np_c$] may produce a substantially different situation:

$$p_\infty + p_c = \frac{1}{n}\rho_\infty c_\infty^2 = \frac{1}{nM_\infty^2}\rho_\infty u_\infty^2 \tag{27}$$

From Eq. (27),

$$\frac{1}{2}\rho_\infty u_\infty^2 = \frac{n}{2}M_\infty^2(p_\infty + p_c)$$

and thus

$$p_\infty \pm \frac{\rho_\infty u_\infty^2}{2}\mathcal{O}(1) = \left\{1 \pm \frac{nM_\infty^2}{2}\left(1 + \frac{p_c}{p_\infty}\right)\mathcal{O}(1)\right\} p_\infty$$

Again, for smooth subsonic flows changing from p_∞ to

$$p_\infty + \frac{\rho_\infty u_\infty^2}{2}\mathcal{O}(1)$$

with sufficient grid points N, then $\Pi_{k+1/2}$ becomes

$$\Pi_{k+1/2} \approx \frac{p_\infty\left\{1 + \frac{nM_\infty^2}{2}(1 + \frac{p_c}{p_\infty})\mathcal{O}(1) \times \frac{k}{N}\right\}}{p_\infty\left\{1 + \frac{nM_\infty^2}{2}(1 + \frac{p_c}{p_\infty})\mathcal{O}(1) \times \frac{k+1}{N}\right\}} = \frac{\left\{1 + \frac{nM_\infty^2}{2}(1 + \frac{p_c}{p_\infty})\mathcal{O}(1) \times \frac{k}{N}\right\}}{\left\{1 + \frac{nM_\infty^2}{2}(1 + \frac{p_c}{p_\infty})\mathcal{O}(1) \times \frac{k}{N}\right\} + \frac{nM_\infty^2}{2}(1 + \frac{p_c}{p_\infty})\mathcal{O}(1) \times \frac{1}{N}} \tag{28}$$

For liquid water, p_c is generally $\mathcal{O}(10^8)$–$\mathcal{O}(10^9)$ Pa to consider a large density and a high speed of sound, and thus the range of p_c/p_∞ is $\mathcal{O}(10^3)$ to $\mathcal{O}(10^4)$ with the freestream pressure p_∞ of $\mathcal{O}(10^5)$ Pa. As a result, $\Pi_{k+1/2}$ in the liquid phase is frequently far away from the value of the unit, even for smooth subsonic flow. This problem essentially comes from the large value of p_c, which is not peculiar for the stiffened-fluid EOS. Actually, other EOS for the liquid phase have a term similar to p_c with a similar order of magnitude. For example, Tait's EOS, which is an isothermal version of the stiffened-fluid EOS, has the following term [19]:

$$\left(\frac{p + p_c}{p_0 + p_c}\right) = \left(\frac{\rho}{\rho_0}\right)^n \tag{29}$$

where $n = 7.0$, $p_c = 3.03975 \times 10^8$ Pa, and $\rho_0 = 1000.0$ kg/m^3. As another example, the van der Waals type of cubic EOS can be written in the following form:

$$(p + A)(v - b) = RT \tag{30}$$

where v is a molar volume. If $A = a/v^2$, Eq. (30) is the van der Waals EOS, and if $A = a\alpha(T)/(v^2 + 2bv - b^2)$, the Peng–Robinson EOS can be obtained [20]. The attraction parameter a and the effective molecular volume b are the coefficients calculated from physical properties. In these EOS, A plays a role similar to p_c in the stiffened-fluid EOS. At atmospheric conditions, A of the Peng–Robinson EOS is approximately equal to 1.3×10^9 Pa for liquid water [21]. Actually, $p + p_c$ of Eq. (29) or $p + A$ of Eq. (30) behave like p in the ideal-gas EOS.

The preceding analysis indicates that if the dynamic pressure ($\frac{1}{2}\rho_\infty u_\infty^2$) is very large compared with the freestream pressure p_∞ [in Eq. (27), this means that p_c/p_∞ is very large], there arises a possibility of a large pressure difference across a cell interface, even in smooth continuous flows. The SDST ($\Pi_{1/2}$) of Eq. (24) will then behave incorrectly in the liquid phase: it recognizes a smooth region as a shock region.

To check the pressure-field variation for the subsonic two-phase mixture flow, the ratio defined by Eq. (31) is examined in terms of mass fraction of the gas phase:

$$\text{ratio} = \frac{\frac{1}{2}\rho_\infty u_\infty^2}{p_\infty} \tag{31}$$

As in many engineering problems, the freestream condition is assumed to be atmospheric. Figure 2 shows that the pressure field is changing drastically near the liquid phase (Y_1 is close to zero). This is due to the large density and the high speed of sound in the liquid phase. For example, in the case of subsonic hydrodynamic problems with the freestream condition ($p_\infty = \mathcal{O}(10^5)$ Pa, $\rho_\infty = 10^3$ kg/m^3, and $u_\infty = \mathcal{O}(10^2)$ m/s), the overall change of the pressure field is from the vaporization pressure, typically $\mathcal{O}(10^3)$ to $\mathcal{O}(10^7)$–$\mathcal{O}(10^8)$ Pa. Thus, for all the drastic change in pressure, the pressure field can be smooth without the presence of a shock wave.

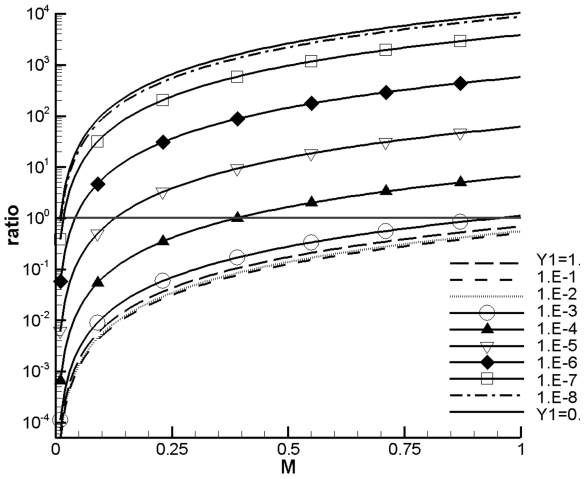

Fig. 2 Ratio (dynamic pressure/freestream pressure) for several mass fractions.

However, the SDST of Eq. (24) does not recognize this physical situation and grossly misinterprets the physically nonshock region as a shock region. The SDST for gas dynamics is clearly inadequate in the region near the liquid phase, and some proper scaling is necessary for robust and accurate computations using the AUSMPW+ and RoeM schemes.

B. Shock-Discontinuity-Sensing for Two-Phase Flow

In the case of gas dynamics, through the analysis of AUSM+ and AUSMD in [13], the density ratio across a cell interface can be chosen as a reference to consider the physical properties on both sides of the cell interface. Assuming the interfacial common speed of sound, the density ratio is then transformed into the pressure ratio to capture contact discontinuity accurately.

In the same manner, we start from the density ratio and change it into the pressure ratio. From the mixture EOS of Eq. (7), the mixture density can be represented by

$$\rho_m = \frac{\partial \rho_m}{\partial p} \Big/ \left(\frac{\alpha_1}{p} + \frac{1 - \alpha_1}{p + p_c}\right) \tag{32}$$

where α_1 is the volume fraction of the gas phase, and p_c is a constant from the liquid-phase EOS. Assuming the interfacial common values of $\partial\rho_m/\partial p$ and volume fraction, we define the following pressure function $\bar{p}_{L,R}$ across the cell interface:

$$\bar{p}_{L,R} = 1 \Big/ \left(\frac{\alpha_{1,1/2}}{p_{L,R}} + \frac{1 - \alpha_{1,1/2}}{p_{L,R} + p_c}\right) \tag{33}$$

where $\alpha_{1,1/2}$ is the volume fraction of the gas phase at a cell interface, which can be obtained from geometrical information or from cell-interface pressure, enthalpy, and mass fraction. In this work, $\alpha_{1,1/2}$ is calculated from cell-interface variables. Then with Eqs. (32) and (33), the ratio of the mixture density can be changed into the pressure ratio:

$$\frac{\rho_{m,L}}{\rho_{m,R}} \approx \frac{\bar{p}_L}{\bar{p}_R} \tag{34}$$

and the following term can be obtained as a new shock-discontinuity-sensing term for two-phase flows:

$$\Pi_{1/2}^* = \min\left(\frac{\bar{p}_L}{\bar{p}_R}, \frac{\bar{p}_R}{\bar{p}_L}\right) \tag{35}$$

where $\bar{p}$ of Eq. (33) is actually a volumetric harmonic average of p in the gas region and $p + p_c$ in the liquid region at the cell interface. The proposed SDST, $\Pi_{1/2}^*$, basically checks the occupied portion of p and $p + p_c$ at a cell interface, which is physically reasonable in the sense that $p + p_c$ in the liquid-phase EOS plays a role similar to p in

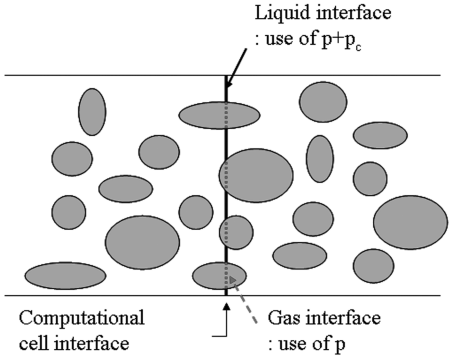

Fig. 3 Geometrical meaning of the new SDST.

the gas-phase EOS. The geometrical meaning of the new SDST is shown schematically in Fig. 3.

To ensure the capability of the new SDST, the behavior of $\Pi^*_{1/2}$ is examined for one-dimensional mixture shock conditions. Table 1 compares the inverse values of the SDST ($\Pi_{1/2}$ and $\Pi^*_{1/2}$) in terms of the mass fraction of the gas phase with $M = 1.5$ and 2.0. Even for the lower-Mach-number case ($M = 1.5$), $\Pi_{1/2}$ near the liquid phase is very large due to the large density and high speed of sound. $\Pi^*_{1/2}$, however, provides well-scaled values throughout the whole range of mass fraction, which indicates that $\Pi^*_{1/2}$ can be used consistently for all mixture flows regardless of the mixture density and speed of sound.

It is possible to apply the proposed strategy to derive a new SDST from other forms of EOS for two-phase flows. For example, if one is interested in isothermal flows, Tait's EOS of Eq. (29) is used for both liquid and gas phases. For the gas phase with the coefficients of $n_1 = 1.4$, $p_{c,1} = 0$, and $\rho_{0,1} = 1.0\ \mathrm{kg/m^3}$, the following density-pressure relation can be derived in a similar manner:

$$\rho_m = \frac{1}{c^2} \Big/ \left(\frac{\alpha_1}{n_1 p} + \frac{1-\alpha_1}{n_2(p + p_{c,2})} \right) \tag{36}$$

From Eq. (36), the same form of $\Pi^*_{1/2}$ can be obtained with the following $\bar{p}_{L,R}$:

$$\bar{p}_{\,L,R} = 1 \Big/ \left(\frac{\alpha_{1,1/2}}{n_1 p_{L,R}} + \frac{1-\alpha_{1,1/2}}{n_2(p_{L,R} + p_{c,2})} \right) \tag{37}$$

According to the authors' experience in isothermal two-phase computations, there was no significant difference between using Eq. (33) and using Eq. (37).

In the case of the Peng–Robinson EOS for liquid water [21] and the ideal-gas EOS for the gas phase, it is not straightforward to obtain a form similar to Eq. (33) or Eq. (37) directly from the complicated EOS. In addition, the coefficient $A(=a\alpha(T)/(v^2 + 2bv - b^2))$ of the Peng–Robinson EOS is not strictly constant. However, the use of $\Pi^*_{1/2}$ with the following $\bar{p}_{L,R}$ is reasonable, because p_c plays a role similar to A in the stiffened EOS, and the value of A does not change notably for liquid water:

$$\bar{p}_{\,L,R} = 1 \Big/ \left(\frac{\alpha_{1,1/2}}{p_{L,R}} + \frac{1-\alpha_{1,1/2}}{p_{L,R} + A_\infty} \right) \tag{38}$$

where A_∞ is the freestream value.

V. Two-Phase Extension of AUSMPW+ and RoeM

A. Two-Phase AUSMPW+ Scheme

The extension of the AUSMPW+ scheme to two-phase flow starts from the basic form of AUSMPW+ for gas dynamics:

$$E_{1/2} = \bar{M}^+_L c_{1/2} Q^*_L + \bar{M}^-_R c_{1/2} Q^*_R + (P^+_L p_L + P^-_R p_R) \tag{39}$$

where $\bar{M}^+_L$ and $\bar{M}^-_R$ are exactly the same as in Eq. (13), and the advection variable vector is defined as

$$Q^* = [\rho_m, \rho_m u, \rho_m v, \rho_m H, \rho_m Y_1]^T \tag{40}$$

In this work, the pressure-based weighting functions ω and $f_{L,R}$ are defined by

$$\omega = \max(\omega_1, \omega_2) \tag{41}$$

$$f_{L,R} = \left(\frac{\bar{p}_{L,R}}{\bar{p}_s} - 1 \right) \times (1 - \omega) \tag{42}$$

with $\omega_1 = 1 - \Pi^{*3}_{1/2}$ and

$$\omega_2 = 1 - \left(\frac{\min(\bar{p}_{L,1}, \bar{p}_{R,1}, \bar{p}_{L,2}, \bar{p}_{R,2})}{\max(\bar{p}_{L,1}, \bar{p}_{R,1}, \bar{p}_{L,2}, \bar{p}_{R,2})} \right)^2$$

where ω_2 is introduced to robustly treat single- or two-phase multidimensional shocks by feeding a proper amount of additional numerical dissipation [22].

The first modification in Eq. (39) is obviously the use of $\Pi^*_{1/2}$ and $\bar{p}$ in the pressure-based weight functions ω and $f_{L,R}$. Because ω has the role of stabilizing the scheme near the shock region, $\Pi^*_{1/2}$ in ω helps shock-sensing capability for two-phase flows. Similarly, $f_{L,R}$ plays the role of providing the pressure-field information to the density field, as will be seen in Eqs. (44) and (45), and the use of $\bar{p}$ in $f_{L,R}$ makes the dissipation term related to pressure difference suitably scaled for two-phase flows.

The second modification is about the definition of the numerical speed of sound $c_{1/2}$. Because there is no Prandtl-like relation across a phase interface, the speed of sound at the phase interface is physically indeterminate and it has to be approximated based on the two-phase-flow physics. For the physical phase interface shown in Fig. 4a and for the computational mesh 1 shown in Fig. 4b, the speed of sound at the cell containing the phase interface would be lower than that of either side, because the mixture EOS at the cell yields a lower sound speed. Thus, it is consistent with the assumption of the HEM to assume a lower sound speed than that of either phase when the computational cell interface is aligned with the phase interface, as shown in Fig. 4c. This property (the lower speed of sound at the phase interface) can be satisfied if the interfacial speed of sound is

Table 1 Inverse values of the SDSTs for the 1-D shock relation (subscript L indicates preshock value)

$p_L = 101325$ Pa				$M_L = 1.5$		$M_L = 2.0$	
Mass fraction	α_L	$\rho_{m,L}$ kg/m^3	c_L m/s	$1/\Pi_{1/2}$	$1/\Pi^*_{1/2}$	$1/\Pi_{1/2}$	$1/\Pi^*_{1/2}$
$Y_1 = 0.0$ (pure liquid)	0.0	1000.00	1458.95	6565.685	3.18750	15756.3	6.25000
$Y_1 = 1.0 \times 10^{-8}$	8.163×10^{-6}	999.99	1347.99	4836.944	2.61162	12682.5	5.22595
$Y_1 = 1.0 \times 10^{-7}$	8.163×10^{-5}	999.92	885.63	8.24318	1.22860	2494.80	1.83307
$Y_1 = 1.0 \times 10^{-6}$	8.157×10^{-4}	999.19	342.81	2.42609	2.06508	4.84434	2.78550
$Y_1 = 1.0 \times 10^{-5}$	8.097×10^{-3}	991.91	112.01	2.26608	2.22898	4.06936	3.83132
$Y_1 = 1.0 \times 10^{-4}$	7.548×10^{-2}	924.61	38.10	2.25124	2.24752	4.00529	3.98094
$Y_1 = 1.0 \times 10^{-3}$	0.4497	550.87	20.23	2.24981	2.24943	3.99909	3.99665
$Y_1 = 1.0 \times 10^{-2}$	0.8918	109.25	32.26	2.25005	2.25001	3.99940	3.99915
$Y_1 = 1.0 \times 10^{-1}$	0.9891	12.12	92.31	2.25426	2.25426	4.00948	4.00946
$Y_1 = 1.0$ (pure gas)	1.0	1.225	340.29	2.45833	2.45833	4.50000	4.50000

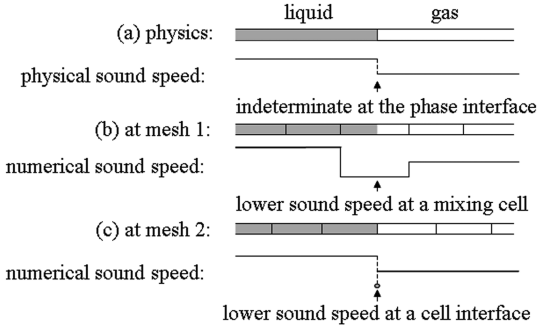

Fig. 4 Physical and numerical sound speed.

calculated from some averaged mass or volume fraction on both sides. In this work, $c_{1/2}$ is obtained from a Roe-type density-weighted enthalpy and mass fraction:

$$c_{1/2} = c_{1/2}(p_{1/2}, \hat{h}_m, \hat{Y}_1) \tag{43}$$

where $p_{1/2}$ is a simple arithmetic average of left and right pressure. Also note that $\alpha_{1,1/2}$ used in $\bar{p}_{L,R}$ of Eq. (33) is evaluated in the same manner: that is, $\alpha_{1,1/2} = \alpha_{1,1/2}(p_{1/2}, \hat{h}_m, \hat{Y}_1)$.

As long as $c_{1/2}$ satisfies the property mentioned previously, other choices of $c_{1/2}$ are allowable without significant difference. It is noted, however, that $c_{1/2}$ obtained from a simple combination of the left and right sound speed, such as $c_{1/2} = (c_L + c_R)/2$ or $c_{1/2} = \min(c_L, c_R)$, cannot satisfy the property when a phase interface is aligned with a cell interface. With these values, some numerical instability can be triggered in two-phase problems, including rapid phase interface, such as liquid-shock/gas-bubble interaction or underwater-explosion problems. With the $c_{1/2}$ formulated as in Eq. (43), AUSMPW+ may lose the one-cell shock-capturing property, which was guaranteed in gas dynamics. However, it does not affect the resolution of the slip line.

With the two modifications, AUSMPW+ can solve mixture flows or two-phase flows with a small density difference. For two-phase flows with a large density ratio, however, serious numerical instability can be encountered.

For $0 \le M_{1/2} \le 1$, the numerical dissipation of AUSMPW+ can be expressed by

$$\begin{aligned} D_{\text{AUSMPW+}} &= \left\{ U_R + \frac{c_{1/2}}{2}(M_R - 1)^2 \omega (1 + f_R) \right\} \Delta Q^* \\ &+ \frac{U_R + U_L}{2c_{1/2}} Q_L^* \Delta U + \frac{c_{1/2}}{2}(M_R - 1)^2 Q_L^* \Delta f \\ &- (P_L^+ p_L + P_R^- p_R) \end{aligned} \tag{44}$$

where $E_{1/2} = \frac{1}{2}(E_L + E_R) - D$. By the definition of $f_{L,R}$ in Eq. (42), Δf can be written as

$$\Delta f = \frac{p_L p_R + \alpha_{1,1/2} p_c (p_R + p_L) + \alpha_{1,1/2} p_c^2}{p_L p_R + \alpha_{1,1/2} p_c (p_R + p_L) + \alpha_{1,1/2}^2 p_c^2} \times \frac{\Delta p}{\bar{p}_s} \times (1 - \omega) \tag{45}$$

Equation (45) explicitly shows the role of Δp in Δf. With the help of the pressure-based weight function $f_{L,R}$, AUSMPW+ possesses the flux by pressure difference in the mass flux, as in the Roe-type schemes. The advection property Q_L^* of Eq. (44) which includes the mixture density, is multiplied by Δf. If the pressure difference coincides with a large-density-ratio phase interface, the flux induced by pressure difference ($Q_L^* \Delta f$) becomes too large, causing numerical instability. To stabilize the scheme near the large-density-ratio phase interface, the function $f_{L,R}$ is modified by considering density difference on both sides:

$$f_{L,R}^* = \left(\frac{\bar{p}_{L,R}}{\bar{p}_s} - 1 \right) \times (1 - \omega) \times \frac{\min(\rho_{m,L}, \rho_{m,R})}{\rho_{m,L/R}} \tag{46}$$

where

$$(\,)_{L/R} = \begin{cases} (\,)_L, & M_{1/2} \ge 0 \\ (\,)_R, & M_{1/2} < 0 \end{cases}$$

With the modified $f_{L,R}^*$, the numerical dissipation of AUSMPW+ in mass flux becomes

$$\begin{aligned} D_{\text{AUSMPW+}}^{(\rho_m)} &= \left\{ U_R + \frac{c_{1/2}}{2}(M_R - 1)^2 \omega (1 + f_R) \right\} \Delta \rho_m \\ &+ \frac{U_R + U_L}{2c_{1/2}} \rho_{m,L} \Delta U + \frac{c_{1/2}}{2}(M_R - 1)^2 \min(\rho_{m,L}, \rho_{m,R}) \Delta f \end{aligned} \tag{47}$$

Compared with the RoeM dissipation flux equation (48), it is seen that the dissipation term due to pressure difference in Eq. (47) is well-scaled:

$$D_{\text{RoeM}}^{(\rho_m)} = (g\hat{U} + (1 - g)\hat{c}) \Delta \rho_m + \frac{\hat{U}}{\hat{c}} \hat{\rho}_m \Delta U + gf \left(\frac{1}{\hat{c}} - \frac{\hat{U}}{\hat{c}^2} \right) \Delta p \tag{48}$$

Consequently, modifications in developing the two-phase AUSMPW+ can be summarized as follows:

l) A new SDST directly from the two-phase EOS is introduced.

2) The numerical speed of sound at a cell surface is modified.

3) The function $f_{L,R}$ to treat phase interface with a large density ratio is modified.

If the two-phase AUSMPW+ is applied to gas-dynamic flows, it goes back to the perfect-gas version, except for the definition of $c_{1/2}$ in Eq. (43) and a slight change in $f_{L,R}^*$. As a result, AUSMPW+ may lose the one-cell shock-capturing property. This loss is unavoidable because there is no Prandtl-like relation for general two-phase flows. Other characteristics such as total enthalpy conservation, slip-line capturing, and improvements in numerical overshoot/oscillation are still preserved.

B. Two-Phase RoeM Scheme

In compressible two-phase flows, the derivation of the system Jacobian matrix using conservative variables is very complicated because of the mixture EOS. Moreover, due to the high speed of sound at the liquid phase, two-phase-flow analysis usually requires a preconditioning technique, which alters the governing system into a primitive variable-based form. The primitive variable-based Roe scheme can be written as

$$\begin{aligned} E_{1/2} &= \tfrac{1}{2}(E_L + E_R - \Gamma_{e,1/2} |\Gamma_e^{-1} A_p|_{1/2} \Delta Q_p) \\ &= \tfrac{1}{2}(E_L + E_R - \Gamma_{e,1/2} |\tilde{A}(Q_L, Q_R)|_{1/2} \Delta Q_p) \\ &= \tfrac{1}{2}(E_L + E_R - \Gamma_{e,1/2} X |\Lambda| X^{-1} \Delta Q_p) \end{aligned} \tag{49}$$

where the transformation matrix $\Gamma_e = (\partial Q / \partial Q_p)$, and the flux Jacobian matrix via primitive variables $A_p = \partial E / \partial Q_p$. Roe-averaged quantities are used for the interfacial matrices, which can be computed as follows:

In method 1, Roe-averaged quantities for density, velocity, total enthalpy, and mass fraction are first obtained as in gas dynamics. Then the interfacial pressure can be evaluated from Eq. (7) using Newton–Raphson iteration at the expense of extra computational cost.

For efficient computations without compromising accuracy, the following strategy can be used. In method 2, Roe-averaged quantities for velocity, total enthalpy, and mass fraction are evaluated. The interfacial pressure is then approximated as the arithmetic average of left and right pressures, and then the Roe-averaged density can be obtained.

Strictly speaking, the interfacial pressure and density obtained by method 2 are not Roe-averaged quantities. However, due to its simplicity and efficiency, method 2 is adopted in this work. No significant difference was observed between the two methods.

The derivation process of the two-phase RoeM is almost the same as that of gas-dynamic flows [12]. The first step is to convert the Roe scheme into a HLLE-like form.

For the supersonic region, Eq. (49) becomes

$$E_{1/2} = \tfrac{1}{2}[E_L + E_R - \tilde{M} A_p \Delta Q_p] \tag{50}$$

where $\tilde{M} = \text{sign}(\hat{M}) \times \min(1, |\hat{M}|)$ and

$$\hat{M} = \frac{\hat{U}}{\hat{c}} = \frac{n_x \hat{u} + n_y \hat{v}}{\hat{c}}$$

The properties with the hat symbol indicate Roe-averaged values. The remaining numerical dissipation part is

$$\tilde{M} A_p \Delta Q_p - \Gamma_{e,1/2} |\Gamma_e^{-1} A_p|_{1/2} \Delta Q_p = \left(\tilde{M} A_p - \Gamma_{e,1/2} |\Gamma_e^{-1} A_p|_{1/2}\right) \Gamma_e^{-1} \Delta Q \tag{51}$$

Then the eigenvalues of $(\hat{M} A_p - \Gamma_{e,1/2} |\Gamma_e^{-1} A_p|_{1/2}) \Gamma_{e,1/2}^{-1}$ for the subsonic region are as follows:

$$\lambda_{1,2} = \hat{c}(\hat{M}^2 - 1) \qquad \lambda_{3,4,5} = \hat{c}(\hat{M}^2 - 1) + \hat{c}(1 - |\hat{M}|) \tag{52}$$

With the two common parts $\hat{c}(\hat{M}^2 - 1)$ and $\hat{c}(1 - |\hat{M}|)$ of the eigenvalues, the numerical dissipation of Eq. (51) can be grouped into two parts, resulting in the following HLLE-like form of the Roe scheme:

$$E_{1/2} = \tfrac{1}{2}[E_L + E_R - \tilde{M} A_p \Delta Q_p + \hat{c}(\tilde{M}^2 - 1) \Gamma_e \Delta Q_p + \hat{c}(1 - |\tilde{M}|) B \Delta Q] \tag{53}$$

$$B \Delta Q = \left(\Delta \rho_m - \frac{\Delta p}{\hat{c}_m^2}\right) \begin{pmatrix} 1 \\ \hat{u} \\ \hat{v} \\ \hat{H} \\ \hat{Y}_1 \end{pmatrix} + \hat{\rho}_m \begin{pmatrix} 0 \\ \Delta u - n_x \Delta U \\ \Delta v - n_y \Delta U \\ \Delta H - \hat{U} \Delta U - \frac{\Delta p}{\hat{\rho}_m} \\ \Delta Y_1 \end{pmatrix} \tag{54}$$

Following the idea of the RoeM scheme for gas dynamics [12], we introduce the Mach-number-based control functions f and g to balance the feeding and damping rates of pressure-density coupling in the continuity equation:

$$E_{1/2} = \frac{1}{2}[E_L + E_R - \tilde{M} A_p \Delta Q_p + \hat{c}(\tilde{M}^2 - 1) \Gamma_e \Delta Q_p + g \hat{c}(1 - |\tilde{M}|) B \Delta Q] \tag{55}$$

$$B \Delta Q = \left(\Delta \rho_m - f \frac{\Delta p}{\hat{c}^2}\right) \begin{pmatrix} 1 \\ \hat{u} \\ \hat{v} \\ \hat{H} \\ \hat{Y}_1 \end{pmatrix} + \hat{\rho}_m \begin{pmatrix} 0 \\ \Delta u - n_x \Delta U \\ \Delta v - n_y \Delta U \\ \Delta H - \hat{U} \Delta U - \frac{\Delta p}{\hat{\rho}_m} \\ \Delta Y_1 \end{pmatrix} \tag{56}$$

Equations (55) and (56) are the two-phase shock-stable RoeM scheme. The control functions f and g are defined as follows:

$$f = \begin{cases} 1 & \hat{u}^2 + \hat{v}^2 = 0 \\ |\hat{M}|^h & \hat{u}^2 + \hat{v}^2 \neq 0 \end{cases} \tag{57}$$

$$g = \begin{cases} |\hat{M}|^{1 - \Pi_{1/2}^*} & \hat{M} \neq 0 \\ 1 & \hat{M} = 0 \end{cases} \tag{58}$$

where

$$h = 1 - \min(\Pi_{1/2}^*, \Pi_{L,1/2}^*, \Pi_{L,-1/2}^*, \Pi_{R,1/2}^*, \Pi_{R,-1/2}^*)$$

and the new SDST is used in f and g.

To satisfy the total-enthalpy-conservation condition in steady flows, $D^{\text{energy}} = D^{\text{mass}} \times H$, Eqs. (55) and (56) can be changed as follows:

$$E_{1/2} = \tfrac{1}{2}[E_L + E_R - \tilde{M} A_p \Delta Q_p + \hat{c}(\tilde{M}^2 - 1) \Delta Q^* + g \hat{c}(1 - |\tilde{M}|) B \Delta Q^*] \tag{59}$$

$$B \Delta Q^* = \left(\Delta \rho_m - f \frac{\Delta p}{\hat{c}^2}\right) \begin{pmatrix} 1 \\ \hat{u} \\ \hat{v} \\ \hat{H} \\ \hat{Y}_1 \end{pmatrix} + \hat{\rho}_m \begin{pmatrix} 0 \\ \Delta u - n_x \Delta U \\ \Delta v - n_y \Delta U \\ \Delta H \\ \Delta Y_1 \end{pmatrix} \tag{60}$$

$$Q^* = [\rho_m, \rho_m u, \rho_m v, \rho_m H, \rho_m Y_1]^T \tag{61}$$

By introducing the signal velocities to prevent expansion shock without compromising the capturing capability of contact discontinuity, the final two-phase RoeM scheme is summarized as follows:

$$E_{1/2} = \frac{1}{b_1 - b_2}\left[b_1 \times E_L - b_2 \times E_R + b_1 \times b_2 \times \left(\Delta Q^* - \frac{g}{1 + |\tilde{M}|} B \Delta Q^*\right)\right] \tag{62}$$

where $b_1 = \max(\hat{U} + \hat{c}, U_R + \hat{c}, 0)$ and $b_2 = \min(\hat{U} - \hat{c}, U_L - \hat{c}, 0)$.

VI. Preconditioned AUSMPW+ and RoeM

As the flow Mach number becomes lower, most upwind-based schemes lose their accuracy and robustness unless the formulation of numerical flux is modified to take into account the preconditioned-system eigenvalues. In other words, the numerical dissipation of upwind schemes in a low-Mach-number region should be scaled by local velocity magnitude, rather than by the speed of sound. In this section, all-speed versions of the two-phase AUSMPW+ and RoeM are introduced.

In preconditioning the upwind schemes, the discrete equation by the preconditioned scheme should consistently represent the continuum counterpart in the incompressible limit by properly scaling numerical dissipation. Guillard and Viozat [23] analyzed the original and the preconditioned Roe schemes in the incompressible limit. Recently, Liou [24] analyzed the AUSM$^+$up scheme for a low-Mach-number limit and designed a proper scaling of diffusion terms. In this section, the preconditioning of the two-phase AUSMPW+ and RoeM schemes is first carried out, and asymptotic analysis is introduced to examine the incompressible-limit characteristics of the preconditioned two-phase AUSMPW+ and RoeM schemes by employing the approach in [23,24]. The summary of the asymptotic analysis is given in the Appendix.

A. Preconditioning of the Two-Phase AUSMPW+ Scheme

According to the previous studies on the preconditioning of AUSM-type schemes by Edwards and Liou [14] for gas dynamics and by Edwards et al. [5] for two-phase flows, there have been three major issues in the preconditioning of AUSM+ and AUSMDV. The first is the scaling issue to reflect the preconditioned-system eigenvalues. Because AUSMPW+ shares the concept of the Mach number splitting function with other AUSM-type schemes, we adopt the same scaling technique in [14] for the scaling of the Mach number and speed of sound:

$$E_{1/2} = \bar{M}_L^{*+} c_{1/2}^* Q_L^* + \bar{M}_R^{*-} c_{1/2}^* Q_R^* + \left(P_L^{*+} p_L + P_R^{*-} p_R\right) \tag{63}$$

In Eq. (63), $\bar{M}^{*\pm}_{L,R}$ and $P^{*\pm}_{L,R}$ indicate the Mach number splitting functions using the following scaled Mach number:

$$M^{**}_{L,R} = \frac{1+M^2_{r,1/2}}{2}\times\frac{M_{L,R}}{\phi_{1/2}} + \frac{1-M^2_{r,1/2}}{2}\times\frac{M_{R,L}}{\phi_{1/2}} \tag{64}$$

where $M^2_r = c'^2/c^2$ and

$$\phi_{1/2} = \frac{\sqrt{(1-M^2_{r,1/2})M^2_{1/2} + 4M^2_{r,1/2}}}{1+M^2_{r,1/2}}$$

are introduced to reflect the preconditioned-system eigenvalues. The scaled interfacial speed of sound is

$$c^*_{1/2} = c_{1/2}\times\phi_{1/2} \tag{65}$$

The second issue is the treatment of the pressure-velocity coupling at low speed. Because the first scaling enforces AUSM-type schemes to behave more like a central-differencing scheme as the Mach number is getting smaller, there is a possibility of the odd–even decoupling. However, AUSMPW+ already has a pressure-velocity coupling term through the control function, $f_{L,R}$. Thus, a simple scaling of $f_{L,R}$ is enough for the second issue. From Eqs. (45), (47), and (65), the numerical dissipation related to Δp in the mass flux becomes smaller as the Mach number is lowered:

$$\begin{aligned}&\frac{c^*_{1/2}}{2}(M^{**}_R - 1)^2\min(\rho_{m,L},\rho_{m,R})\Delta f\\ &\quad\rightarrow \mathcal{O}(U)\times\mathcal{O}(\rho_m)\times\frac{\Delta p}{\mathcal{O}(\bar{p})}\times\mathcal{O}(1)\rightarrow\mathcal{O}(U)\times\frac{\Delta p}{\mathcal{O}(c^2)}\times\mathcal{O}(1)\end{aligned} \tag{66}$$

In low-Mach-number flows, $O(c^2)$ is too large compared with Δp, and thus the pressure-velocity coupling could be too small. Thus, $\mathcal{O}(c^2)$ is scaled to $\mathcal{O}(c'^2)$ for the odd–even decoupling problem:

$$\begin{aligned}f^{**}_{L,R} &= f^*_{L,R}\times\frac{1}{M^2_r} = \left(\frac{\bar{p}_{L,R}}{\bar{p}_s} - 1\right)\times(1-\omega)\\ &\quad\times\frac{\min(\rho_{m,L},\rho_{m,R})}{\rho_{m,L/R}}\times\frac{1}{M^2_r}\end{aligned} \tag{67}$$

The last issue is about the calculation of the liquid phase. For the two-phase AUSMPW+ scheme, however, the scaling problem that arises from the calculation of different phases is already cured by $\Pi^*_{1/2}$ and $\bar{p}$ in the pressure-based weight functions ω and $f_{L,R}$. With the preceding modifications, AUSMPW+ for all Mach number two-phase flows is obtained.

B. Preconditioning of the Two-Phase RoeM Scheme

The preconditioned two-phase Roe scheme can be written as

$$E_{1/2} = \tfrac{1}{2}(E_L + E_R - \Gamma_{1/2}|\Gamma^{-1}A_p|_{1/2}\Delta Q_p) \tag{68}$$

The direct derivation of a preconditioned RoeM from the form of Eq. (68) is quite complicated because of the eigenvalues of the subsonic dissipation. Thus, we implement the Harten–Lax–van Leer with contact restoration (HLLC)-type preconditioning strategy by Luo et al. [15] into the RoeM scheme. By scaling the numerical dissipation of the RoeM scheme using the preconditioned eigenvalues appearing in Eq. (5), the preconditioning of the RoeM in Eq. (59) can be efficiently realized as follows:

$$\begin{aligned}E_{1/2} &= \tfrac{1}{2}[E_L + E_R - \tilde{M}^*\Delta E + \hat{D}(\tilde{M}^{*2}-1)\Delta Q^*\\ &\quad + g\hat{D}(1-|\tilde{M}^*|)B\Delta Q^{**}]\end{aligned} \tag{69}$$

$$B\Delta Q^{**} = \left(\Delta\rho_m - f\frac{\Delta p}{\hat{D}^2}\right)\begin{pmatrix}1\\ \hat{u}\\ \hat{v}\\ \hat{H}\\ \hat{Y}_1\end{pmatrix} + \hat{\rho}_m\begin{pmatrix}0\\ \Delta u - n_x\Delta U\\ \Delta v - n_y\Delta U\\ \Delta H\\ \Delta Y_1\end{pmatrix} \tag{70}$$

where $\tilde{M}^* = \text{sign}(\hat{M}^*)\times\min(1,|\hat{M}^*|)$ and $\hat{M}^* = \hat{U}'/\hat{D}$. $\hat{U}'$ and $\hat{D}$ have the same from as U' and D in Eq. (5), but with Roe-averaged values. Finally, the all-speed version of the RoeM is obtained from Eq. (62):

$$\begin{aligned}E_{1/2} &= \frac{1}{b^*_1 - b^*_2}\Big[b^*_1\times E_L - b^*_2\times E_R + b^*_1\times b^*_2\\ &\quad\times\left(\Delta Q^* - \frac{g}{1+|\tilde{M}^*|}B\Delta Q^{**}\right)\Big]\end{aligned} \tag{71}$$

where $b^*_1 = \max(\hat{U}' + \hat{D}, U'_L + \hat{D}, 0)$ and $b^*_2 = \min(\hat{U}' - \hat{D}, U'_R - \hat{D}, 0)$.

The computational costs of the proposed schemes with first-order accuracy in time and space are as follows: Roe is 1, AUSMPW+ is 0.97, and RoeM is 1.04.

VII. Numerical Results

We have applied the two-phase AUSMPW+ and RoeM schemes to several mixture/phase-interfacial two-phase problems, ranging from highly compressible to nearly incompressible flow regions. Unless otherwise stated, the third-order total-variation-diminishing Runge–Kutta scheme [25] is used as a time-integration scheme, and the atmospheric pressure and temperature are assumed. For a higher-order extension, the primitive variables of Eq. (2) are extrapolated using the MUSCL approach. We set $a_0 = 1\times10^{10}$ for non-preconditioned compressible test problems in Secs. VII.A–VII.F and the $M = 0.675$ case in in Sec. VII.G. For all Mach number preconditioned test problems, such as low-Mach-number flows in Secs. VII.G and VII.H, we simply set $a_0 = 1.0$.

A. Two-Phase Shock-Tube Problem

The two-phase AUSMPW+ and RoeM schemes are applied to a one-dimensional two-phase shock-tube problem of length 1 on a 200-mesh system. The second-order accuracy is ensured by MUSCL with a van Leer limiter. The initial conditions are as follows:

$$(p,u,Y_1,T)_L = (2\times10^7, 0, 0.5, 300) \qquad x\le 0.5$$
$$(p,u,Y_1,T)_R = (1.5\times10^7, 0, 0.5, 300) \qquad x > 0.5$$

Though the initial mass fraction is the same, the initial volume fraction is different by $\alpha_L = 0.801$ and $\alpha_R = 0.841$ due to the pressure difference. We compare the results of the Roe, RoeM, and AUSMPW+ schemes with a fine-grid computation (the result of the Roe scheme on an 800-mesh system).

After $t = 0$, the contact discontinuity starts to move to the right, the mixture shock propagates to the right, and the expansion fan propagates to the left. The HEM assumes the same temperature across the phase interface if it is located within the same computational cell. Also, the specific heat Cp of the liquid phase is about 4 times larger than that of the gas phase. Thus, the enthalpy change caused by a temperature change is more noticeable in the liquid phase, and the liquid density increases more than that of the gas phase, which causes gas volume-fraction expansion in the low-temperature region. These characteristics are shown in Fig. 5. In this case, all three schemes give almost the same results, indicating that the two-phase AUSMPW+ and RoeM schemes exhibit an accuracy similar to the original two-phase Roe scheme.

B. Quirk's Test with Two-Phase Mixture Flows

A moving shock with the speed of $M = 6$ on a perturbed-mesh system is conducted to examine the shock stability in two-phase mixture flows. The mesh system is 800×20 with unit spacing, and

the centerline is perturbed as follows:

$$y_{i,j_{\text{mid}}} = \begin{cases} y_{j_{\text{mid}}} + 10^{-4} & \text{for } i \text{ even} \\ y_{j_{\text{mid}}} - 10^{-4} & \text{for } i \text{ odd} \end{cases}$$

The first-order flux is used for time integration and spatial discretization.

In Quirk's test for gas dynamics, it is well known that a scheme suffering from the shock-instability phenomenon destroys the original moving-shock profile by amplifying numerical error. Figure 6 shows the results of each scheme for a $Y_1 = 0.1$ mixture flow. Although Roe's FDS destroys the initial normal shock, both the AUSMPW+ and RoeM cleanly capture the shock, showing their robust and shock-stable behavior even in the two-phase-flow region.

The same test was also carried out by changing the mass fraction. The results are summarized in Table 2. The AUSMPW+ and RoeM do not show any shock instability, whereas Roe's FDS exhibits carbuncles, except for near the liquid region. It appears that the large value of p_c in the liquid-phase EOS suppresses the amplifying mechanism of Roe's FDS by loosening the coupling between the density and pressure field. Thus, the shock instability phenomenon of Roe's FDS in two-phase flow can be affected by some additional factors such as the mass fraction or EOS.

C. Test with Two-Phase Mixture Flows

As a tougher test case, the $M = 3$ stationary shock problem by Sanders et al. [26] is examined in mixture flows. Temporal and spatial discretization are first-order-accurate. The mesh system is 100×40 with unit spacing, and the x coordinate of $i = 10$ mesh is perturbed as follows:

$$x_{10,j} = 10 + 0.1\cos(j\pi/10)$$

The computed results are summarized in Table 3, and some selected results are given from Figs. 7–15. Here, the computed result is regarded as stable if there is no evidence of shock breakdown in Mach contour and/or residual blowup. As seen in Table 3, AUSMPW+ and RoeM are shock-stable for all the test cases (see Figs. 8, 9, 11, 12, 14, and 15), though there are some cases with wiggles in Mach contour or with diffusive shock thickness (Fig. 14). However, the Roe scheme yields shock breakdown for the pure gas phase (Fig. 7) or residual blowup for $Y_1 = 0.1$ and $Y_1 = 0.005$ (Fig. 10). Even for near the liquid phase with $Y_1 = 1 \times 10^{-7}$ and $Y_1 = 1 \times 10^{-8}$, the numerical error in the Mach contour is unacceptably large (Fig. 13). However, it is grouped as stable mode 3, because the error does not grow further and is bounded in a shock region. Contrary to the cases of $Y_1 = 1 \times 10^{-7}$ and $Y_1 = 1 \times 10^{-8}$, the residual blows up in cases of $Y_1 = 0.1$ and $Y_1 = 0.005$, even if the Courant–Friedrichs–Lewy (CFL) number is

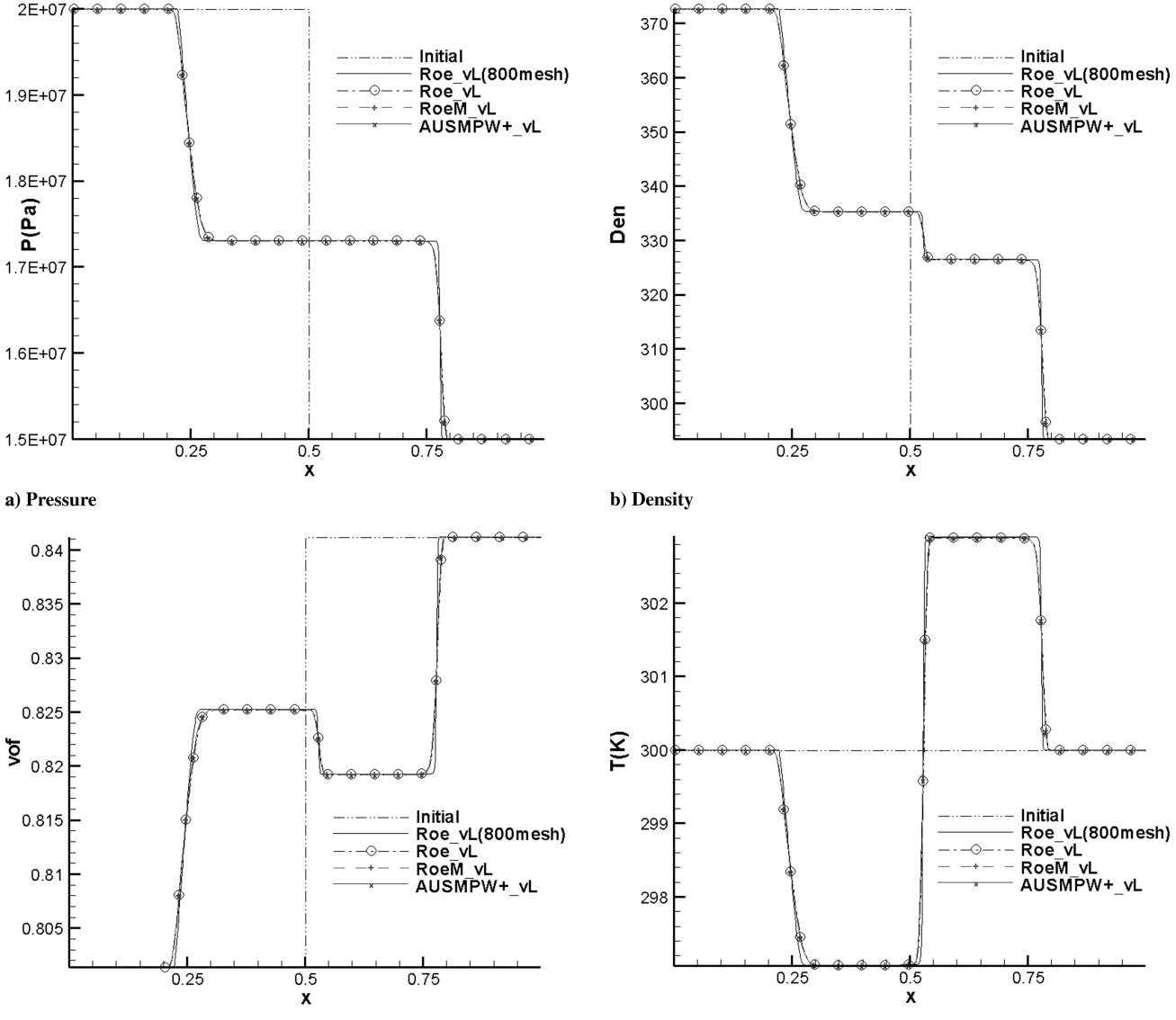

Fig. 5 Shock-tube problem at $t = 1 \times 10^{-4}$.

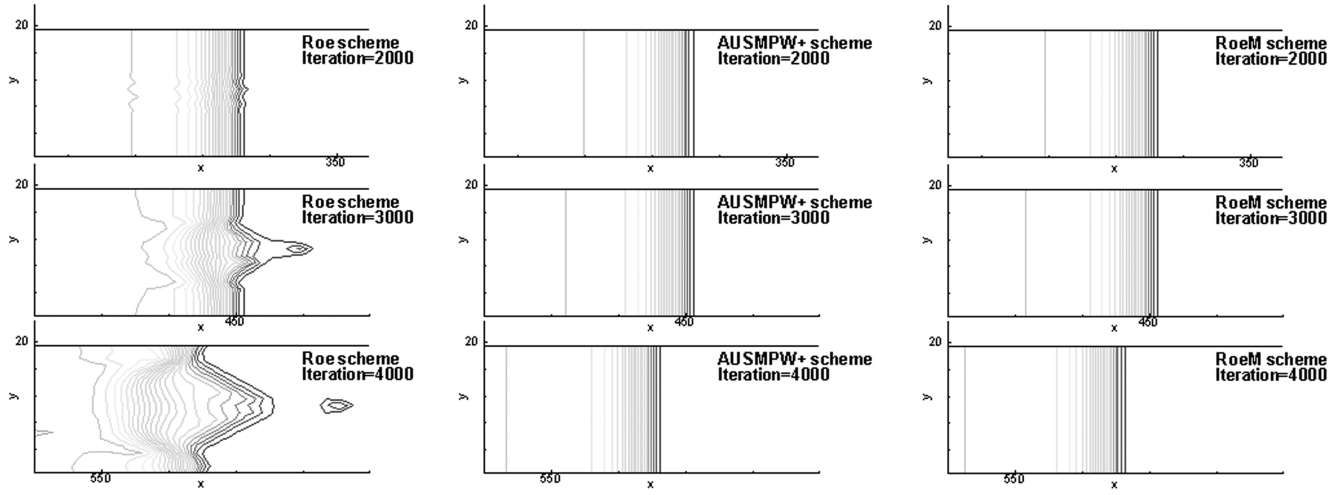

a) Roe **b) AUSMPW+** **c) RoeM**

Fig. 6 Quirk's test on $Y_1 = 0.1$ mixture flow (density contour).

as small as 1.0×10^{-5}. It is observed that the shock breakup mechanism of the original Roe scheme becomes weaker as the flow gets closer to the liquid phase. This is presumably because the coupling between the pressure and density field tends to be loose with a large value of p_c.

D. High-Speed Blunt-Body Flow

A mixture blunt-body flow problem with $M = 8$ and $Y_1 = 0.01$ is chosen as another example to demonstrate the shock-stable characteristic of the two-phase AUSMPW+ and RoeM schemes. Though the freestream Mach number is relatively high, the freestream flow velocity is just about 258.12 m/s, which is not so high, due to the lower speed of sound in mixture flow. We assume that the freestream is at atmospheric conditions and solve the test case on a 51×51 mesh system with the first-order accuracy in time and space.

The original Roe FDS fails again in this test. On the other hand, AUSMPW+ and RoeM solve the high-Mach-number blunt-body problem without any difficulty. Figure 16 shows the results of AUSMPW+ and RoeM. AUSMPW+ shows slight wiggles near the stagnation region in this test case. The stagnation pressure error compared with the theory is −0.644% in AUSMPW+ and +0.095% in RoeM. It is observed that the temperature change across the strong shock is noticeably small due to the high heat capacity of the liquid phase.

Table 2 Summary of Quirk's test with mass fraction

Mass fraction	Roe	AUSMPW+	RoeM
$Y_1 = 0.0$ (pure gas)	Unstable	Stable	Stable
$Y_1 = 1.0 \times 10^{-1}$	Unstable	Stable	Stable
$Y_1 = 1.0 \times 10^{-2}$	Unstable	Stable	Stable
$Y_1 = 5.0 \times 10^{-3}$	Unstable	Stable	Stable
$Y_1 = 1.0 \times 10^{-3}$	Stable	Stable	Stable
$Y_1 = 1.0 \times 10^{-7}$	Stable	Stable	Stable
$Y_1 = 0.0$ (pure liquid)	Stable	Stable	Stable

Table 3 Summary of Sanders et al.'s [26] test with mass fraction[a]

Mass fraction	Roe	AUSMPW+	RoeM
$Y_1 = 0.0$ (pure gas)	Unstable mode 1	Stable mode 1	Stable mode 1
$Y_1 = 1.0 \times 10^{-1}$	Unstable mode 2	Stable mode 1	Stable mode 2
$Y_1 = 5.0 \times 10^{-3}$	Unstable mode 2	Stable mode 1	Stable mode 1
$Y_1 = 1.0 \times 10^{-7}$	Stable mode 3	Stable mode 4	Stable mode 1
$Y_1 = 1.0 \times 10^{-8}$	Stable mode 3	Stable mode 4	Stable mode 1
$Y_1 = 0.0$ (pure liquid)	Stable mode 5	Stable mode 1	Stable mode 1

[a]Stable mode 1 is undeniably stable, stable mode 2 has wiggles in the Mach contour, stable mode 3 errors are bounded in shock, stable mode 4 has diffusive shock thickness, stable mode 5 has with wiggles in density and temperature contour. Unstable mode 1 is the typical instability in Mach contour, and unstable mode 2 is a blow up.

E. Liquid-Shock/Gas-Bubble Interaction

An interaction problem between a liquid shock and a cylindrical air bubble is computed on a 175×125 mesh system. A moving shock of $M = 1.422$ in liquid hits the cylindrical gas bubble with the radius of the unit ($r = 1$). $Y_1 = 1.0$ is initialized for the pure gas phase, and $Y_1 = 0.0$ is initialized for the pure liquid phase. The purpose of this simulation is to demonstrate the capability of the proposed schemes to handle complex two-phase flows. This numerical test can also be thought of as a simplified model of the medical process to eliminate kidney stones using shock waves. To pulverize the kidney stones, a laser-induced shock interacts with a small gas bubble. Then the shock–bubble interaction generates a high-energy explosion and a high-speed liquid jet.

Numerical simulation is carried out by AUSMPW+ and RoeM, and a minmod limiter is used. Figures 17 and 18 show the sequential photographs of the gas-bubble interaction. When the liquid shock hits the gas bubble, it is reflected as a rarefaction wave, whereas the transmitted wave is still a shock (Figs. 17a and 18a). However, when the transmitted shock arrives at the gas–liquid phase interface, both the reflection and transmission waves are all shock waves. Thus, a blast wave is generated at the right end of the gas bubble. In the present simulation, the blast wave is generated at around $t = 0.0024$ and the results in Figs. 17b and 18b are just after explosion. After the bubble collapse, the vortex pair is generated and the high-speed liquid jet is formed (Figs. 17c and 17d). Overall, AUSMPW+ is slightly better at resolving the phase interface, whereas RoeM is slightly better at resolving shock and expansion waves.

Figure 19 is a close-up view of the high-speed liquid jet between the vortex pair. According to the present computation, the jet maintains its structure with the vortex pair until the end of simulation: $t = 0.005$. The maximum velocity of the liquid jet is over 1000 m/s and the initial liquid-shock-induced velocity is 262.16 m/s.

F. Underwater Explosion

This test case is the interaction between the ocean surface and the underwater blast wave. Initially, a gas bubble with $r = 1$ is located at 3 below the ocean surface at $p = 9.12 \times 10^8$ Pa and $\rho = 1270$ kg/m^3. $Y_1 = 1.0$ is initialized for the pure gas phase, and $Y_1 = 0.0$ is initialized for the pure liquid phase. The atmospheric pressure is assumed to be 1.1×10^5 Pa, which is the same initial condition as that of Liu et al. [19]. The simulation is carried out on a 241×241 mesh system, and the multidimensional-limiting-process/van Leer [27] limiter is used to ensure the multidimensional stability.

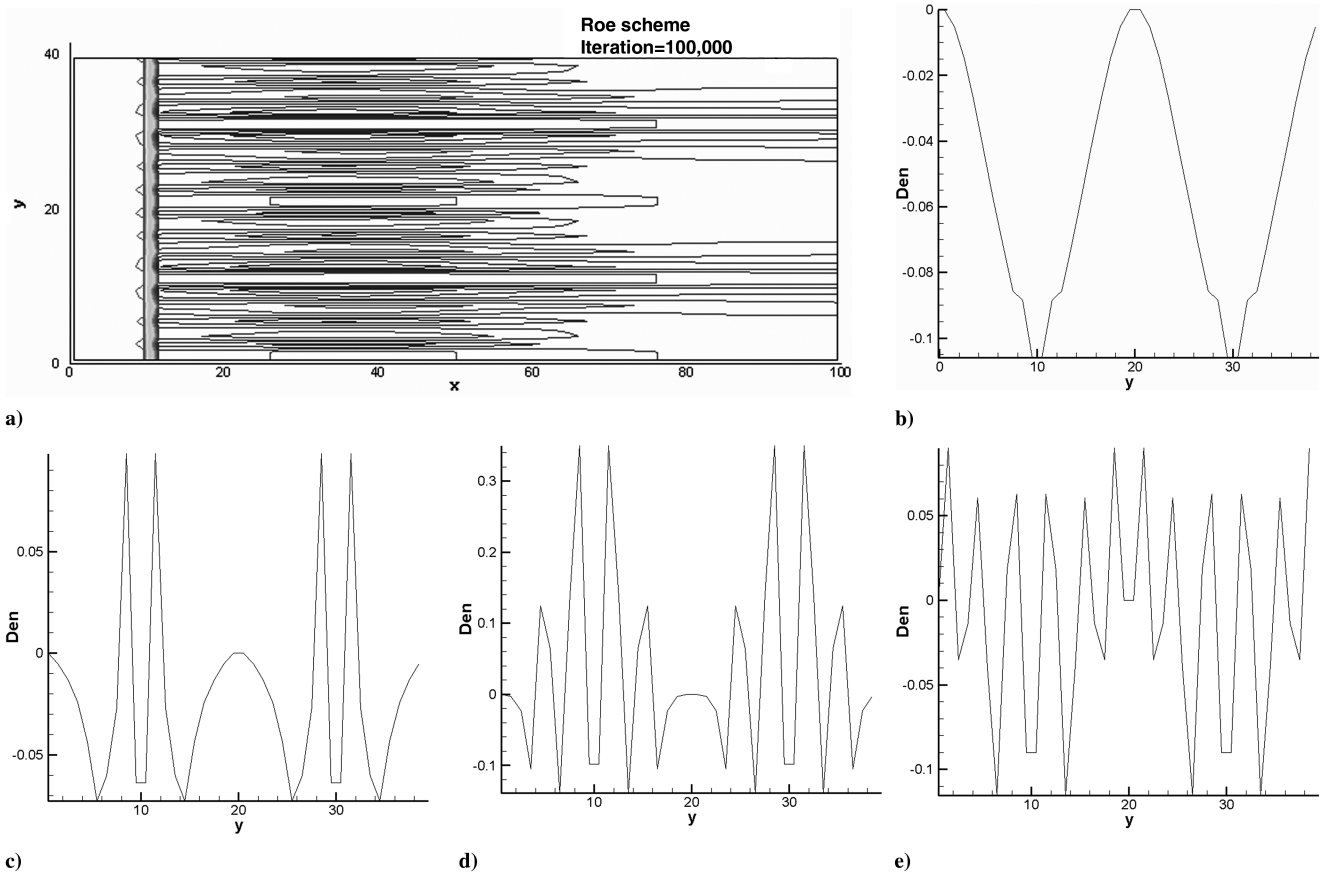

Fig. 7 Sanders et al.'s [26] test on $Y_1 = 1.0$ gas flow with Roe: a) Mach contour with normalized density at $x = 11$ $[(\rho_m(11, y, t) - \rho_m(11, y, 0))/\rho_m(11, y, 0)]$, after b) 10,000 iterations, c) 30,000 iterations, d) 70,000 iterations, and e) 100,000 iterations.

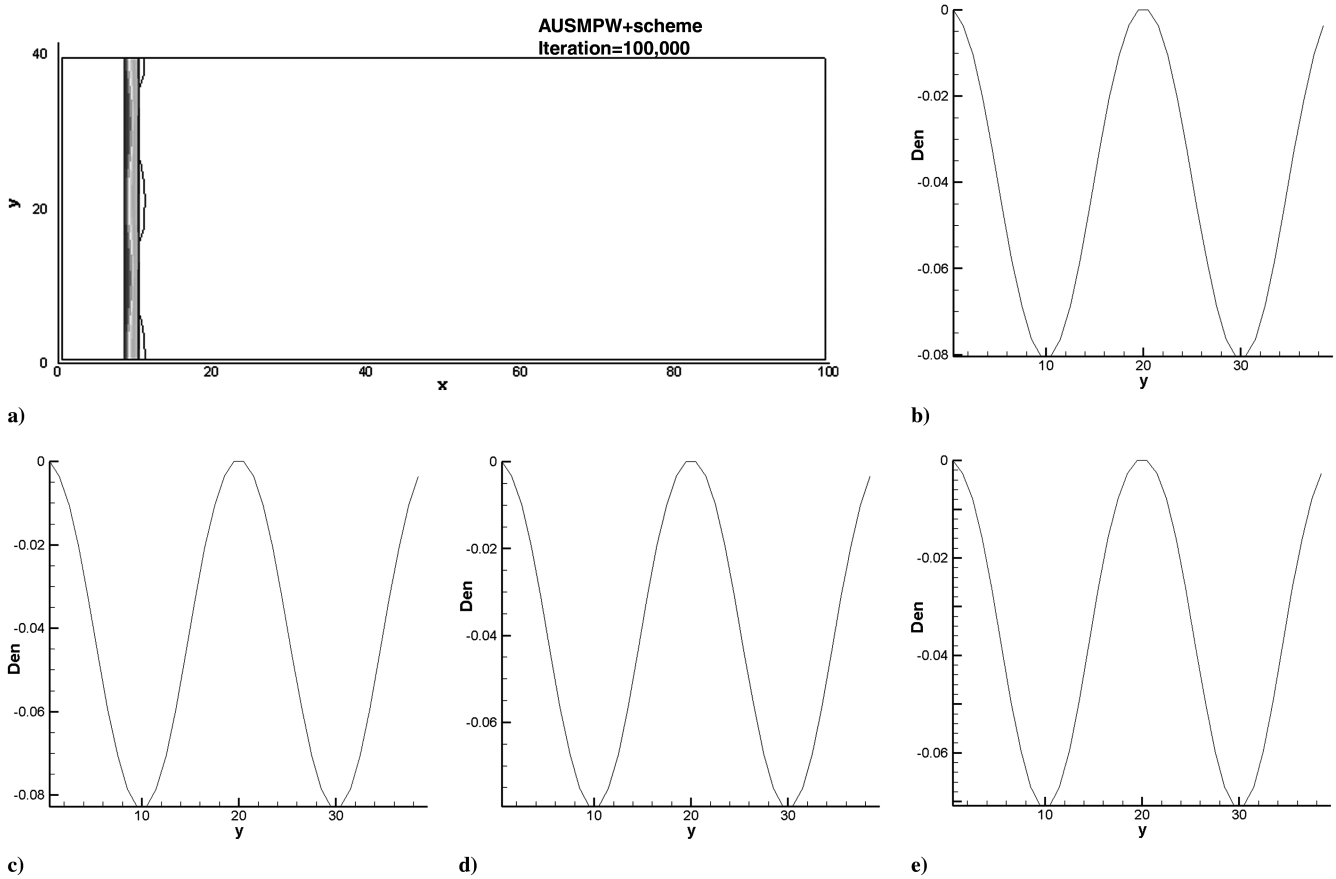

Fig. 8 Sanders et al.'s [26] test on $Y_1 = 1.0$ gas flow with AUSMPW+: a) Mach contour with normalized density at $x = 11$ $[(\rho_m(11, y, t) - \rho_m(11, y, 0))/\rho_m(11, y, 0)]$, after b) 10,000 iterations, c) 30,000 iterations, d) 70,000 iterations, and e) 100,000 iterations.

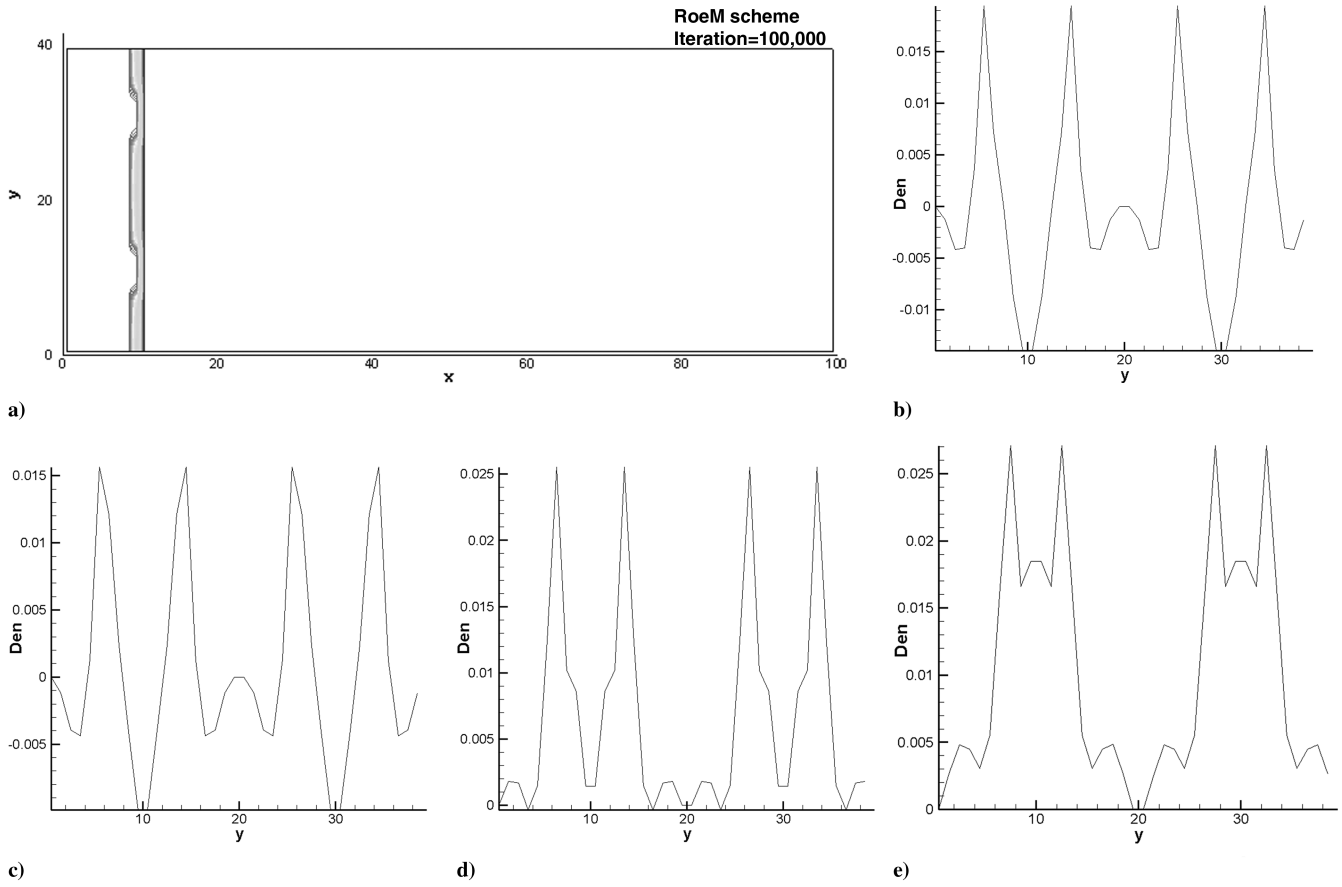

Fig. 9 Sanders et al.'s [26] test on a $Y_1 = 1.0$ gas flow with RoeM: a) Mach contour with normalized density at $x = 11$ $[(\rho_m(11, y, t) - \rho_m(11, y, 0))/\rho_m(11, y, 0)]$, after b) 10,000 iterations, c) 30,000 iterations, d) 70,000 iterations, and e) 100,000 iterations.

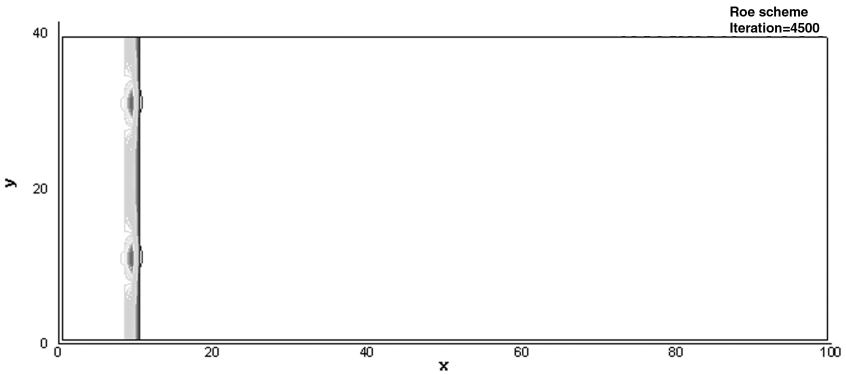

Fig. 10 Mach contour for Sanders et al.'s [26] test on $Y_1 = 0.005$ mixture flow with Roe.

At $t = 0$, the underwater explosion of the high-pressure gas bubble produces a blast wave. When the blast wave reaches the liquid–gas interface, a shock wave is transmitted into the atmosphere and an expansion wave is reflected back into the water region (Fig. 20, $t = 0.0015$). Afterward, the reflected expansion wave interacts with the gas bubble to create a lower-pressure region, and the upper region of the gas bubble accelerates upward (Fig. 20, $t = 0.0025$).

In the close-up view at $t = 0.0025$ in Fig. 21, both schemes show the resultant two-phase wave physics almost identically. The strength of the transmitted shock into the gas (or air) region is very weak compared with the pressure variation in the liquid region, and so the v-velocity contour is plotted to highlight the transmitted shock.

In Fig. 22, we compare the trajectories of the primary waves and interface (shock, phase interface, and the head and tail of expansion waves) with the computed result of Liu et al. [19] and the theory of Ballhaus and Holt [28]. Liu et al. [19] used Tait's EOS for the liquid phase and a wave-physics theory including the phase interface. The theory cannot describe general mixture flows because it considers only the gas–liquid phase interface using the level-set technique. The theoretical result of Ballhaus and Holt [28] is based on the assumption of an axisymmetric explosion and local Taylor expansion, which is valid only for a short period after explosion (see [19,28] for further details).

From the comparison, both AUSMPW+ and RoeM provide very reliable results. Slight variation exists in predicting the transmitted shock into air and the reflected expansion wave formed by the reflection of the main shock from the free surface. But the trajectory and speed of the transmitted shock and the reflected expansion wave lie between the results of Liu et al. [19] and Ballhaus and Holt [28]. The second shock, which is not considered in the work of Ballhaus and Holt, is formed, though the trajectory is somewhat different from the result of Liu et al. [19]. Because Liu et al. used an isothermal EOS

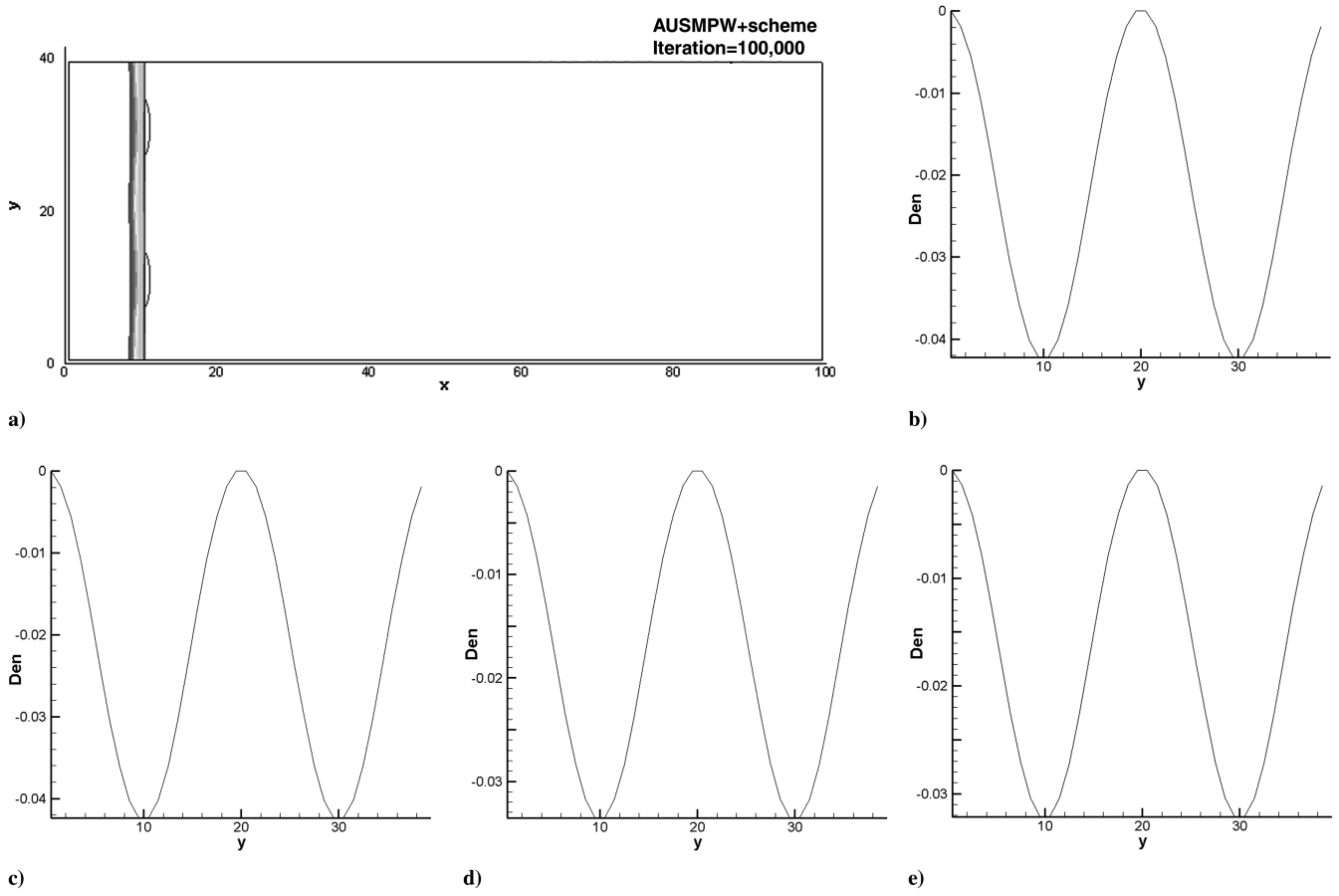

Fig. 11 Sanders et al.'s [26] test on a $Y_1 = 0.005$ mixture flow with AUSMPW+: a) Mach contour with normalized density at $x = 11$ $[(\rho_m(11, y, t) - \rho_m(11, y, 0))/\rho_m(11, y, 0)]$, after b) 10,000 iterations, c) 30,000 iterations, d) 70,000 iterations, and e) 100,000 iterations.

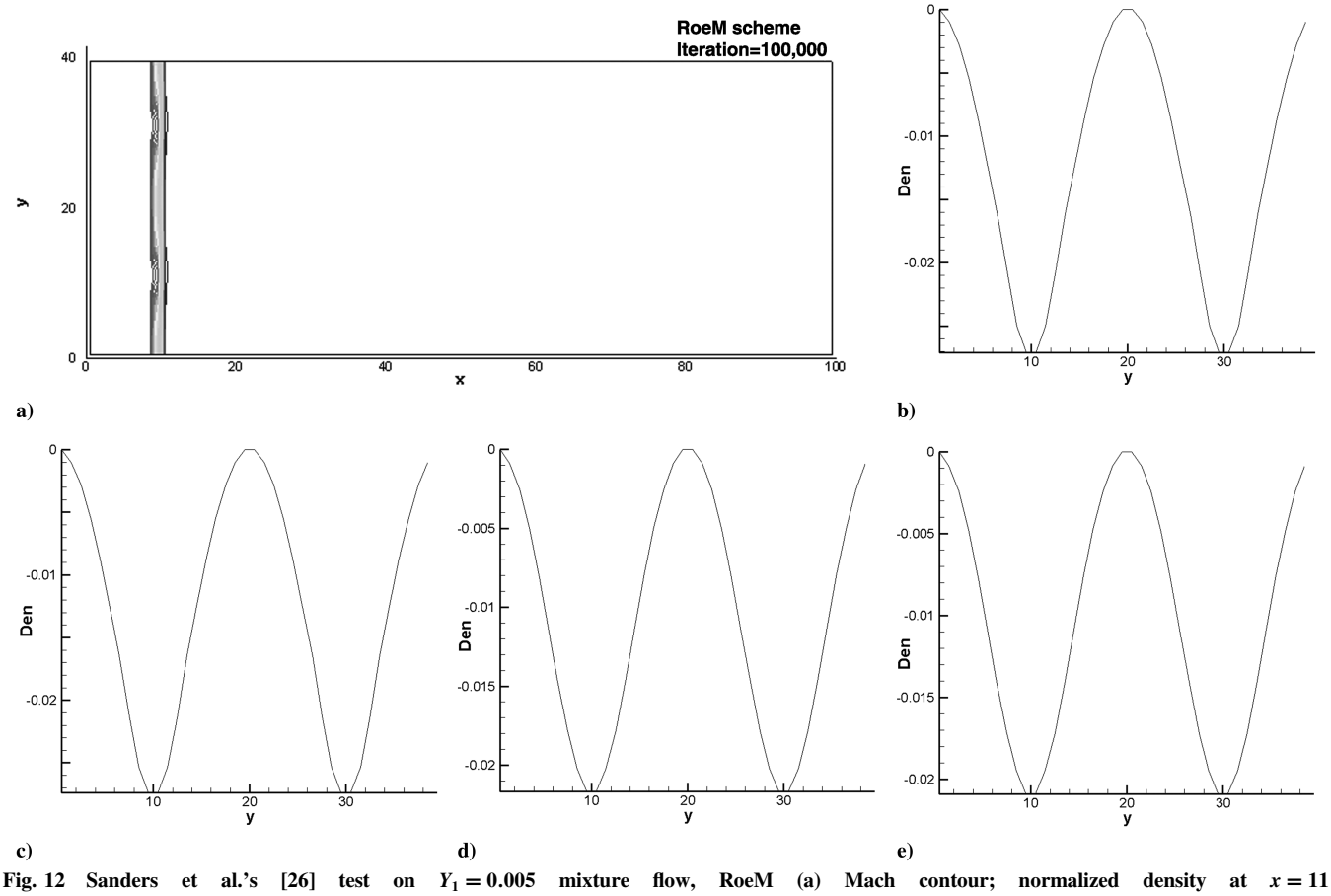

Fig. 12 Sanders et al.'s [26] test on $Y_1 = 0.005$ mixture flow, RoeM (a) Mach contour; normalized density at $x = 11$ $[(\rho_m(11, y, t) - \rho_m(11, y, 0))/\rho_m(11, y, 0)]$, after b) 10,000 iterations, c) 30,000 iterations, d) 70,000 iterations, and e) 100,000 iterations.

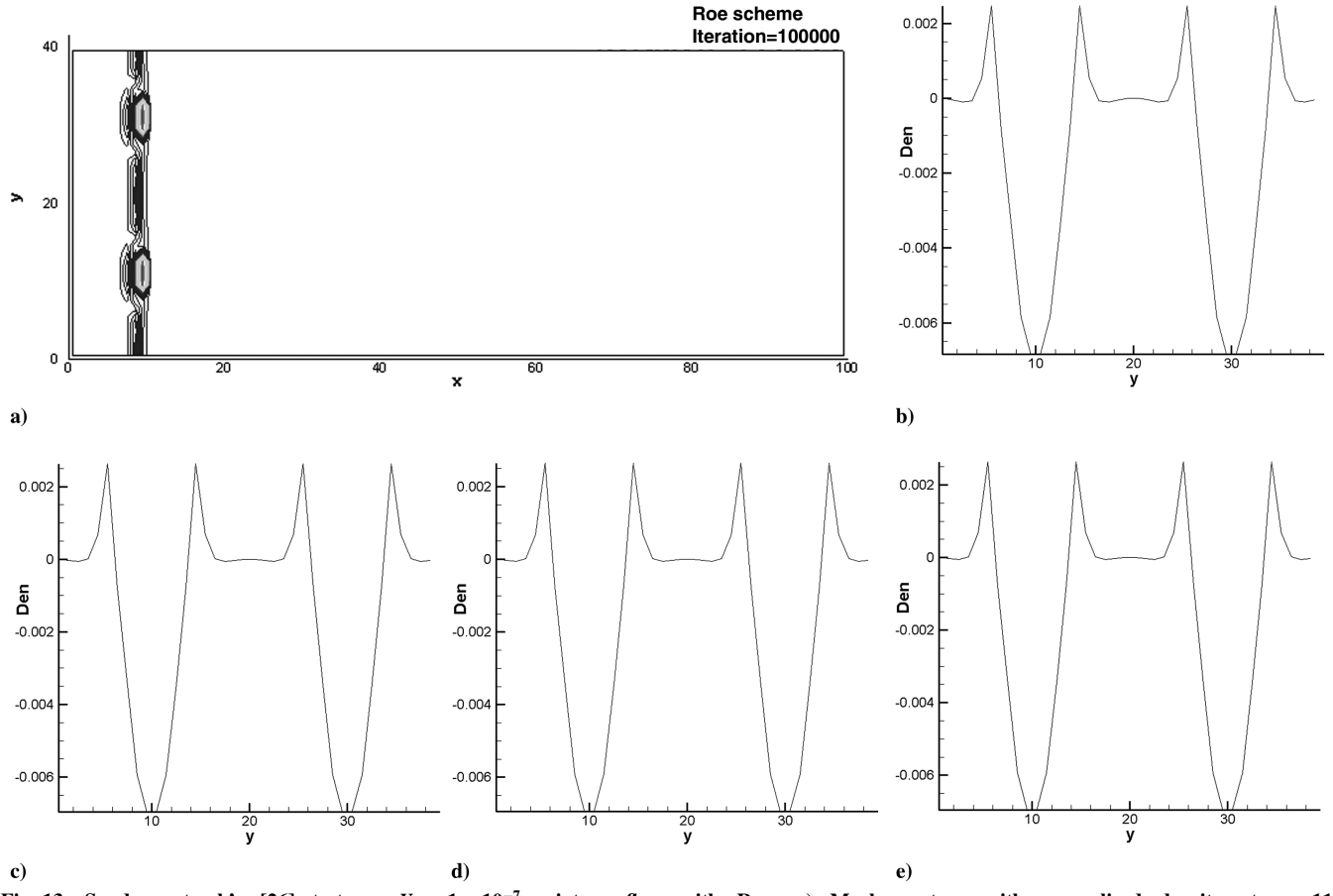

Fig. 13 Sanders et al.'s [26] test on $Y_1 = 1 \times 10^{-7}$ mixture flow with Roe: a) Mach contour with normalized density at $x = 11$ $[(\rho_m(11, y, t) - \rho_m(11, y, 0))/\rho_m(11, y, 0)]$, after b) 10,000 iterations, c) 30,000 iterations, d) 70,000 iterations, and e) 100,000 iterations.

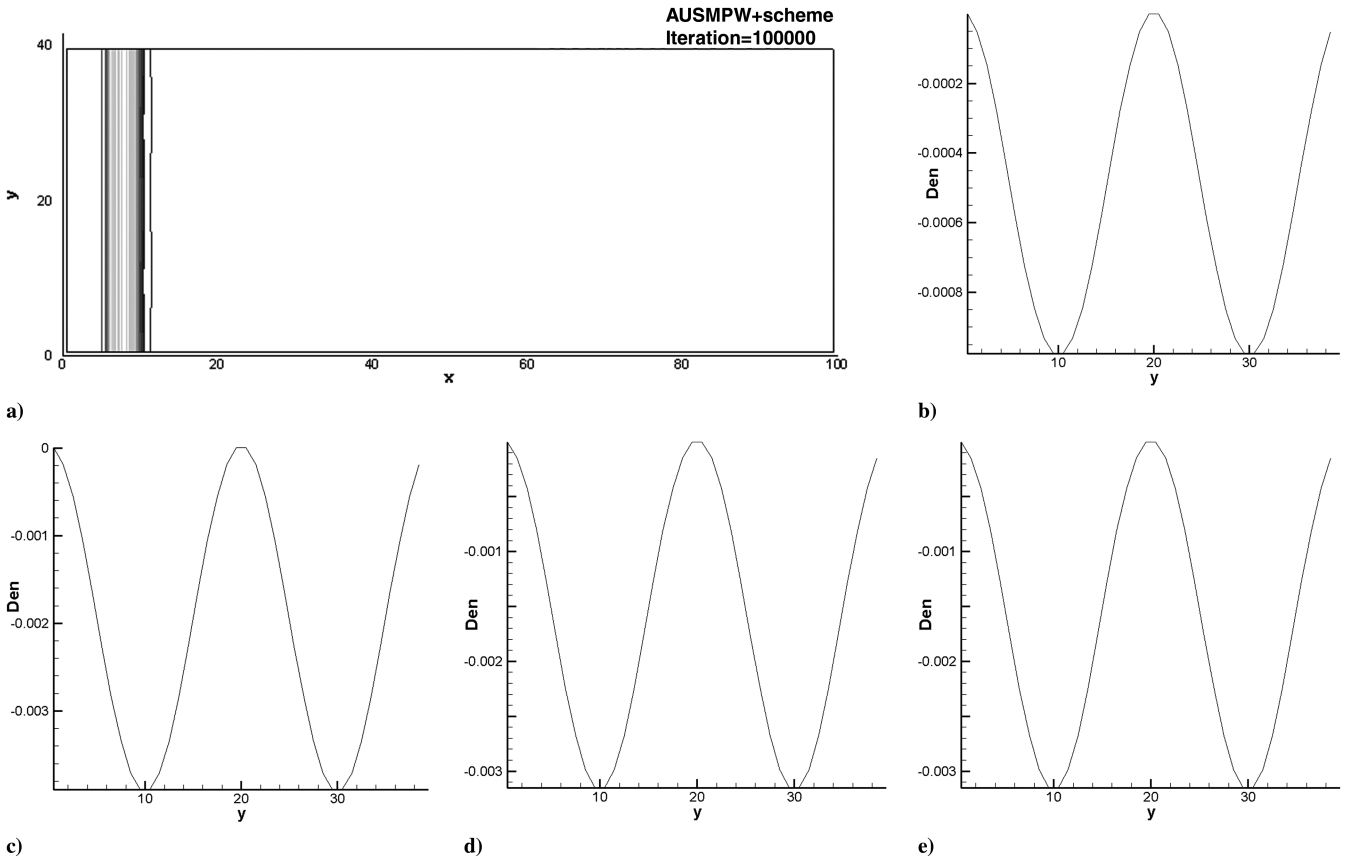

Fig. 14 Sanders et al.'s [26] test on $Y_1 = 1 \times 10^{-7}$ mixture flow with AUSMPW+: a) Mach contour; normalized density at $x = 11$ $[(\rho_m(11, y, t) - \rho_m(11, y, 0))/\rho_m(11, y, 0)]$, after b) 10,000 iterations, c) 30,000 iterations, d) 70,000 iterations, and e) 100,000 iterations.

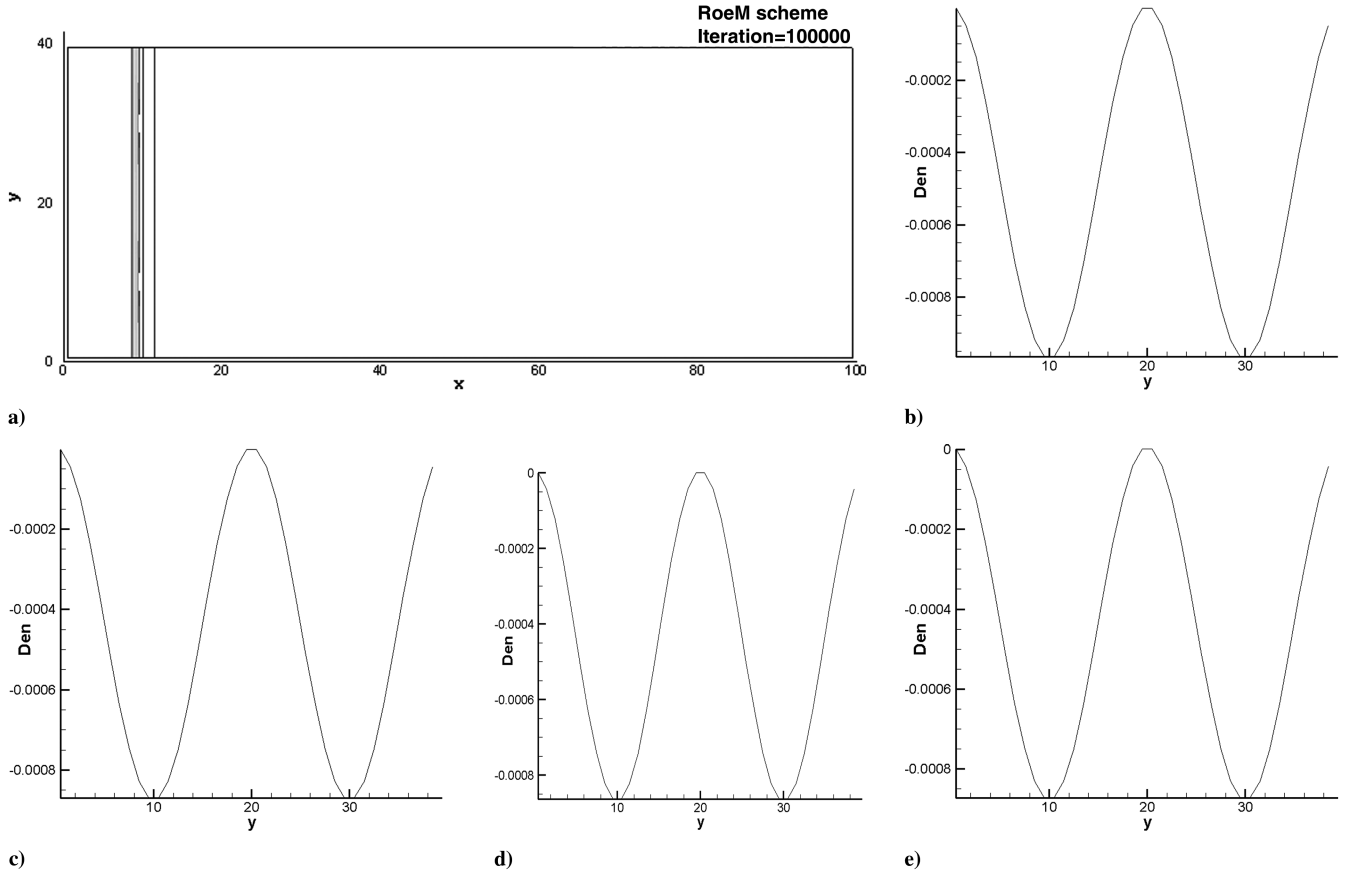

Fig. 15 Sanders et al.'s [26] test on a $Y_1 = 1 \times 10^{-7}$ mixture flow with RoeM: a) Mach contour with normalized density at $x = 11$ $[(\rho_m(11, y, t) - \rho_m(11, y, 0))/\rho_m(11, y, 0)]$, after b) 10,000 iterations, c) 30,000 iterations, d) 70,000 iterations, and e) 100,000 iterations.

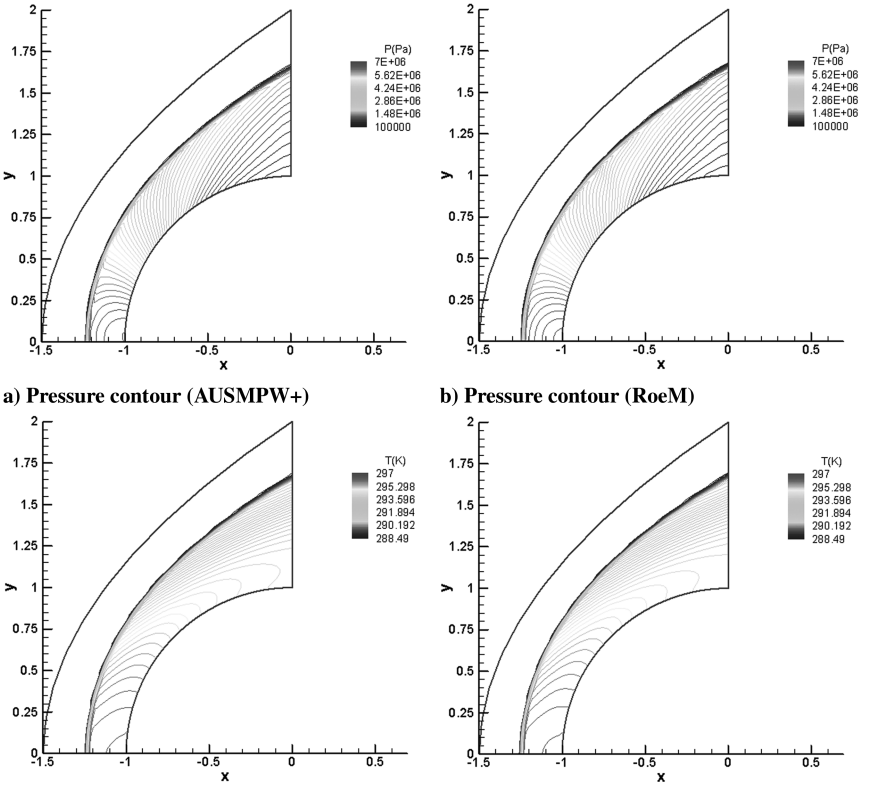

Fig. 16 Mixture blunt-body flow problem ($M = 8$ and $Y_1 = 0.01$): a) pressure contour with AUSMPW+, b) pressure contour with RoeM, c) temperature contour with AUSMPW+, and d) temperature contour with RoeM.

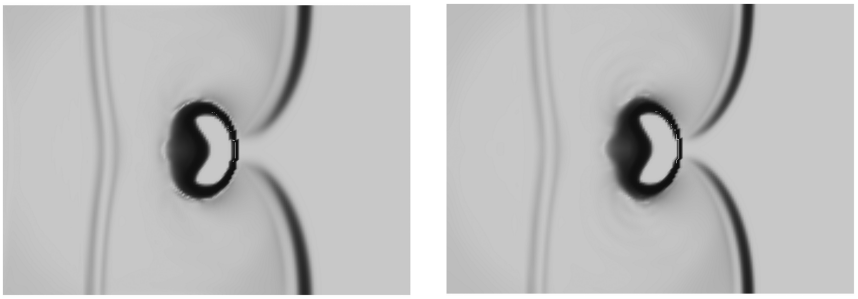

a) AUSMPW+ (left) and RoeM (right) at t = 0.002

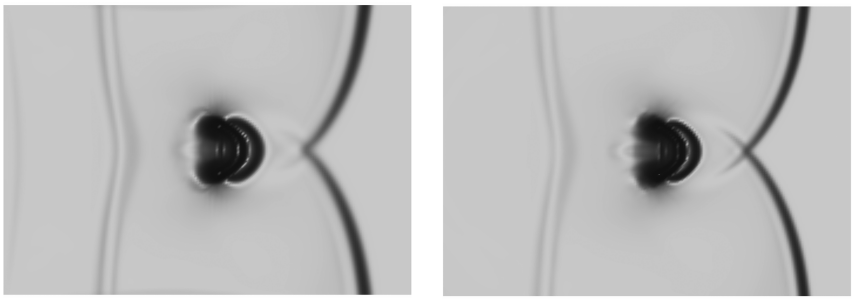

b) AUSMPW+ (left) and RoeM (right) at t = 0.0025

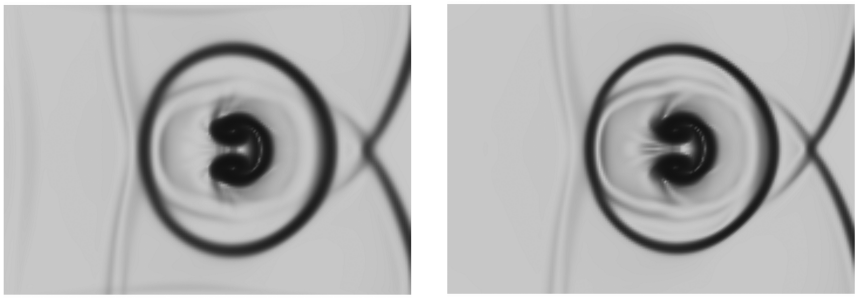

c) AUSMPW+ (left) and RoeM (right) at t = 0.003

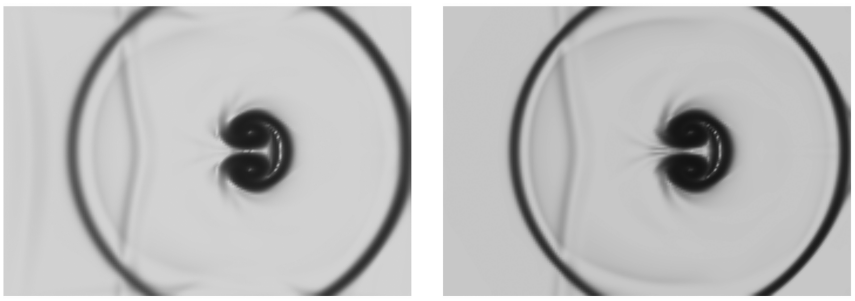

d) AUSMPW+ (left) and RoeM (right) at t = 0.0035

Fig. 17 Numerical schlieren of liquid-shock/gas-bubble interaction for AUSMPW+ (left) and RoeM (right) at a) $t = 0.002$, b) $t = 0.0025$, c) $t = 0.003$, and d) $t = 0.0035$.

for the liquid phase, the heat transfer from the high-temperature gas bubble to the low-temperature surrounding liquid may not be properly delivered. In the present simulation, the temperature around the gas-bubble surface is about 2500 K at $t = 0$, and it is lowered to 1710 K at $t = 0.001$ and is further lowered to about 1265 K at $t = 0.0025$. Thus, the formation and propagation of the second shock is delayed, compared with the result of Liu et al. [19].

G. Mixture-Bump Flow

A two-phase mixture-bump problem is chosen to validate the performance of the proposed schemes at all speeds. A series of mixture flows with $M = 0.675$, 0.01, 1×10^{-4}, and 1×10^{-6} are considered for $Y_1 = 0.1$. The CFL number is 0.8 for $M = 0.675$ and 1.0 for other cases.

Computations are carried out on a 129×65 mesh system, and the results are shown in Fig. 23. Both schemes yield a very similar solution. Oscillations or diffusions, typically seen in the result of low-Mach-number flows using a nonpreconditioned upwind scheme, do not appear. The results for $M = 1 \times 10^{-4}$ and 1×10^{-6} are almost identical to the case of $M = 0.01$.

Convergence histories for the L_2 norm of pressure are shown in Fig. 24. AUSMPW+ and RoeM schemes show similar convergence characteristics. For the case of $M = 1 \times 10^{-6}$, the residuals stall at about 5 orders of magnitude due to the round-off error.

H. Turbulent Cavitation Problem

As a final numerical test, a turbulent cavitating problem over an axisymmetric object with a hemispherical forehead is considered for the cavitation numbers of $Ca = 0.3$ and 0.4 and the Reynolds

number of $Re = 1.36 \times 10^5$. The cavitation model of Merkle et al. [29] is chosen and the standard k-ε model is used. Computation is done on a 121×65 mesh system, and the minmod limiter combined with the dissipation sensor proposed by Kunz et al. [3] is used.

The object initially lies underwater ($Y_1 = 0.0$), and the cavitation phenomenon occurs around the end of the forehead, due to the pressure reduction by flow acceleration. As shown in Fig. 25, the computed results of both schemes match well with the experimental

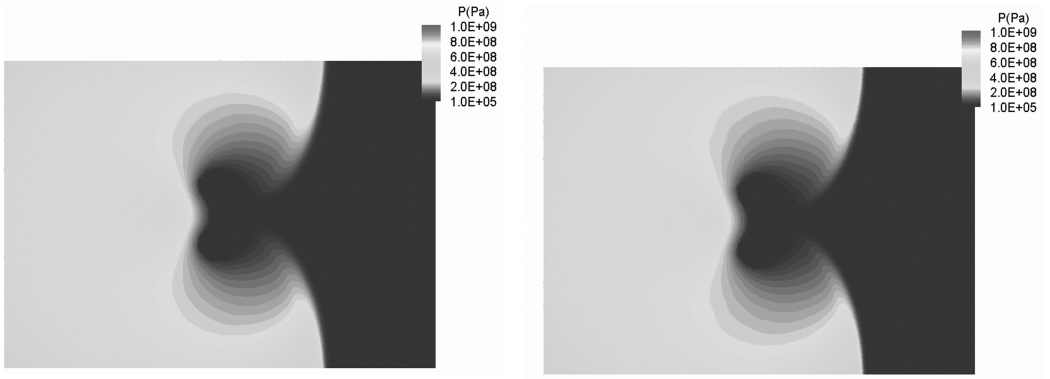

a) AUSMPW+ (left) and RoeM (right) at t = 0.002

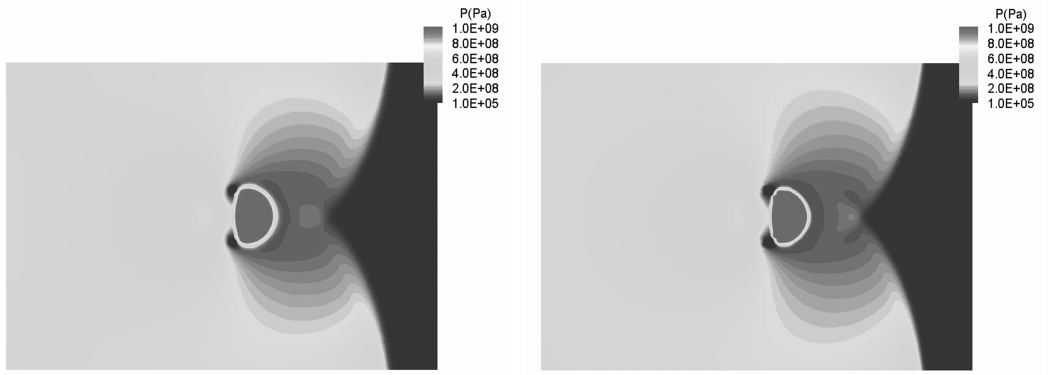

b) AUSMPW+ (left) and RoeM (right) at t = 0.0025

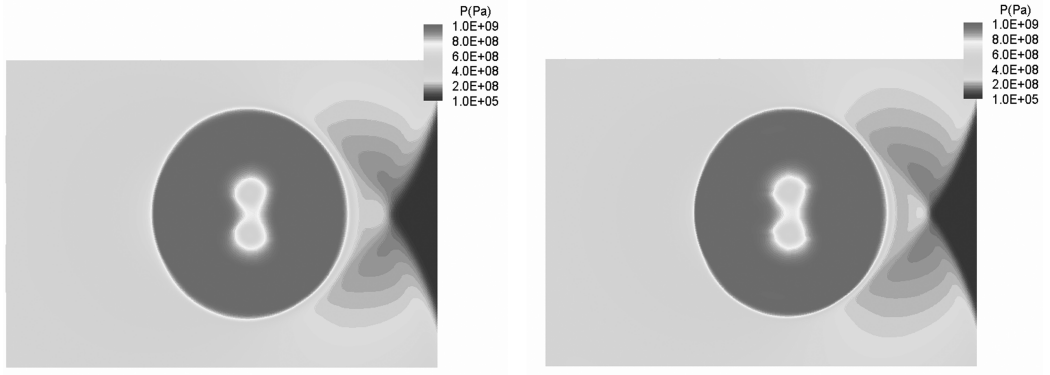

c)) AUSMPW+ (left) and RoeM (right) at t = 0.003

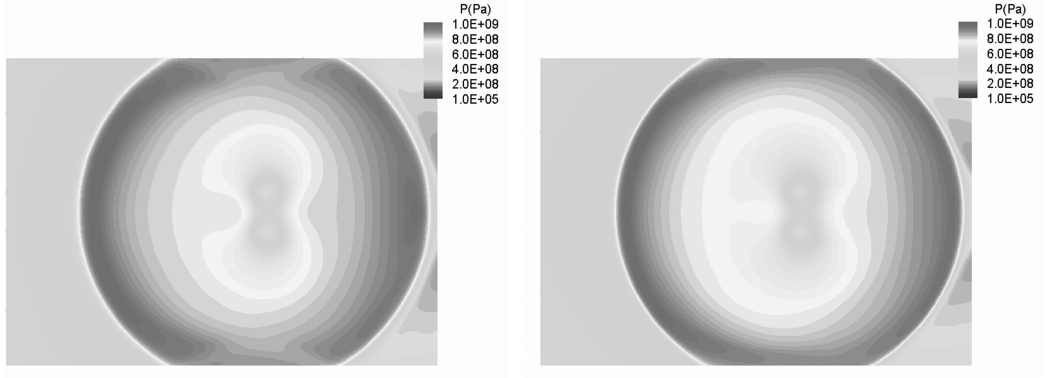

d) AUSMPW+ (left) and RoeM (right) at t = 0.0035

Fig. 18 Pressure contour of liquid-shock/gas-bubble interaction for AUSMPW+ (left) and RoeM (right) at a) $t = 0.002$, b) $t = 0.0025$, c) $t = 0.003$, and d) $t = 0.0035$.

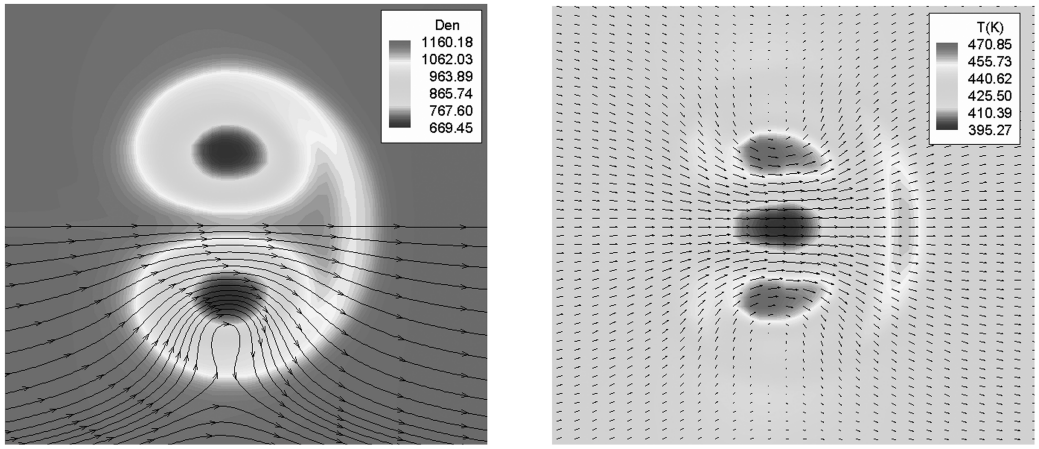

a) Density contour and streamline **b) Temperature contour and velocity vector**

Fig. 19 High-speed liquid jet formation at $t = 0.005$ with RoeM: a) density contour and streamline and b) temperature contour and velocity vector.

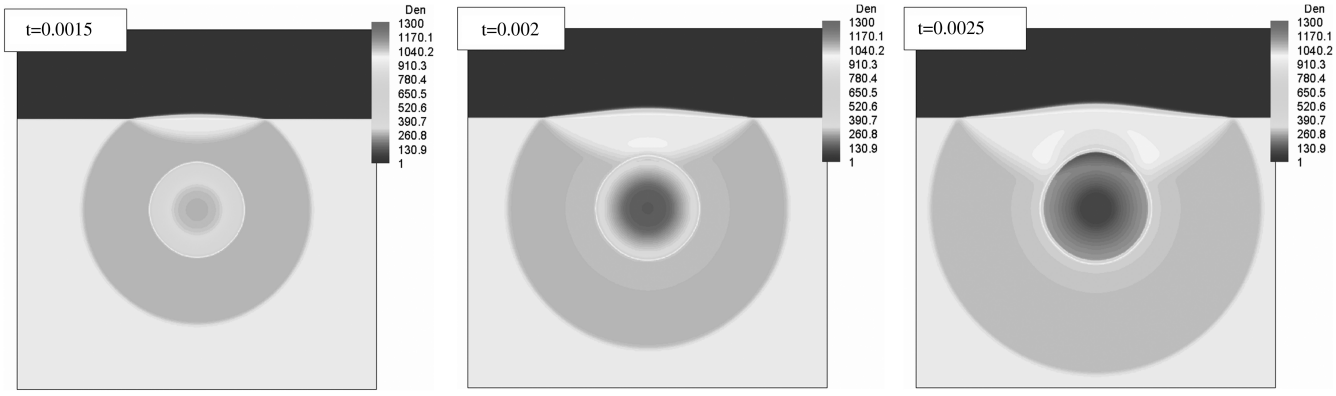

a) Density contour at t = 0.0015, 0.002, 0.0025

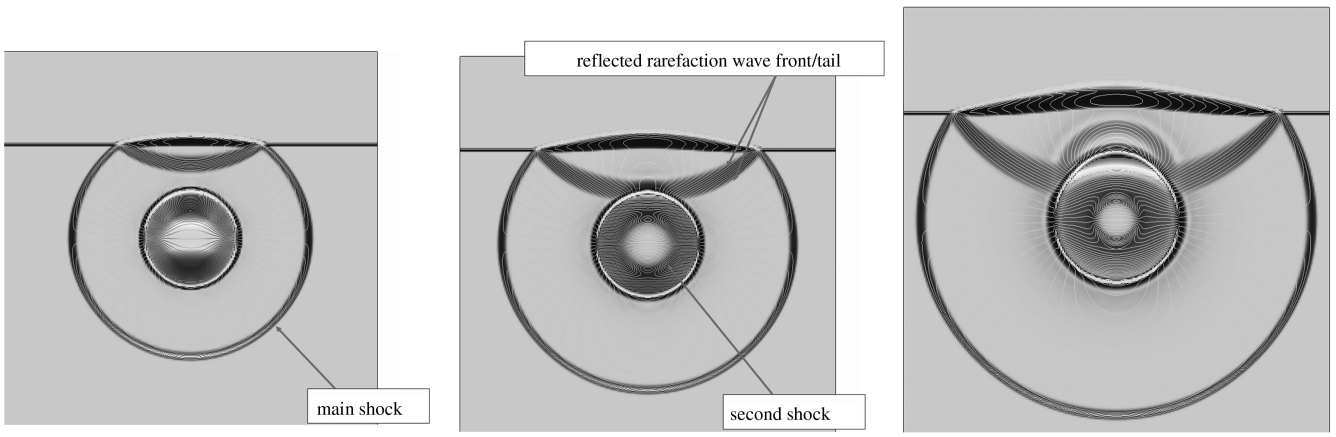

b) Numerical Schlieren and v-velocity contour at t = 0.0015, 0.002, 0.0025

Fig. 20 Underwater explosion with RoeM: a) density contour at $t = 0.0015$, 0.002, and 0.0025 and b) numerical schlieren and v-velocity contour at $t = 0.0015$, 0.002, and 0.0025.

pressure distribution [30]. The formation of cavitation is seen in Fig. 26. It is known that this test case exhibits some degree of unsteadiness, and the surface-pressure distribution can be changed with different grid systems, cavitation models, spartial accuracy, and even with different pressure splitting in AUSM+ [5]. Considering all of these aspects, the difference in the computed pressure between AUSMPW+ and RoeM is acceptable.

In terms of the CFL condition, however, a significant difference is observed between AUSMPW+ and RoeM. The CFL condition of AUSMPW+ is more restrictive, especially at the inception of cavitation, for which the allowable CFL number of AUSMPW+, compared with that of RoeM, was typically reduced from 1/2 to 1/10. Thus, RoeM appears to be more efficient in this class of problem. According to the authors' experiences, RoeM is generally more robust in terms of the CFL condition for the problems involving phase interface.

VIII. Conclusions

Accurate and efficient computations of compressible gas–liquid two-phase flows based on the homogeneous-equilibrium model are conducted. The AUSMPW+ and RoeM schemes, which have been successfully demonstrated in gas dynamics, are extended to homogeneous-equilibrium two-phase flow at all speeds, without

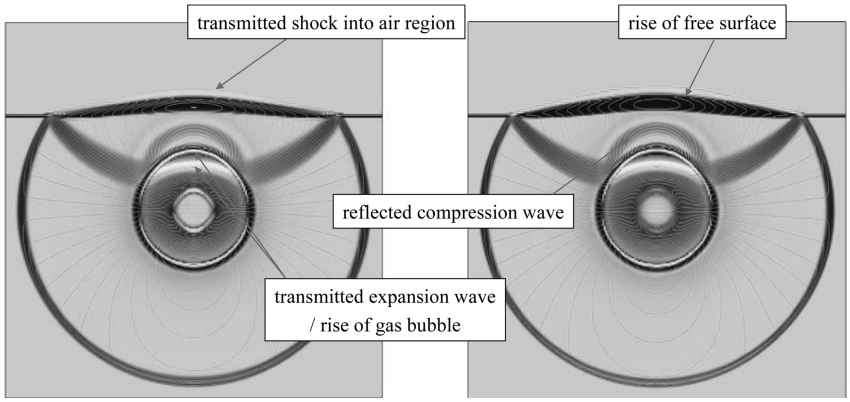

a) AUSMPW+ b) RoeM

Fig. 21 Comparison of the result at $t = 0.0025$: a) AUSMPW+ and b) RoeM.

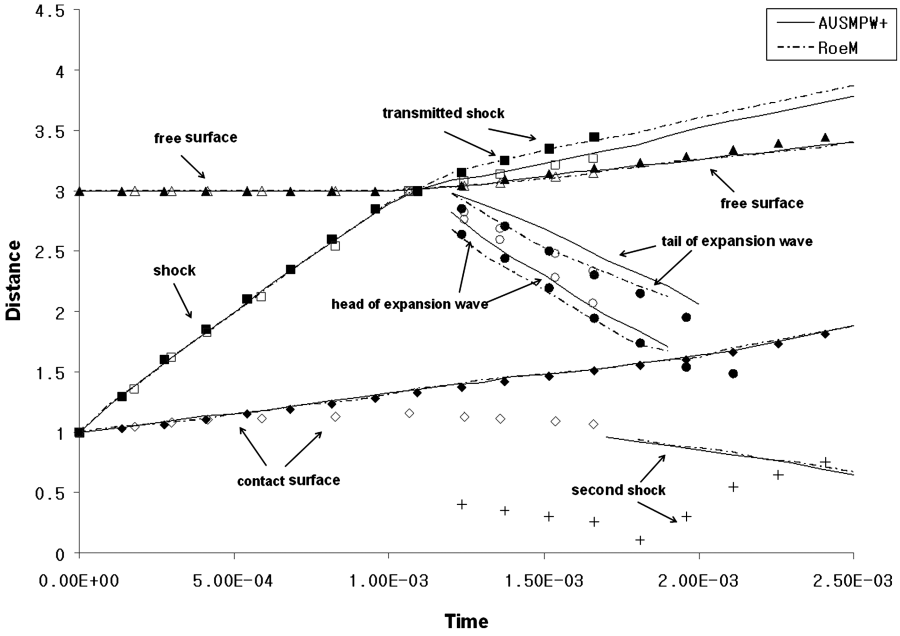

Fig. 22 Discontinuity comparison of the present computation using AUSMPW+(solid line) and RoeM (dotted dashed line) with the Liu et al. [19] computation ▲■●◆) and Ballhaus and Holt [28] theory (△□○◇); *y*-directional distance from the center of the initial gas bubble.

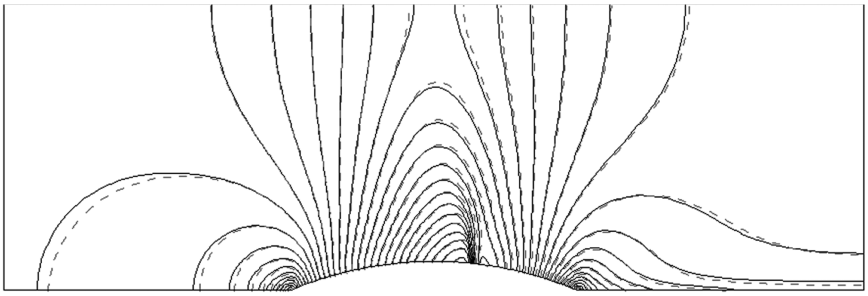

a) $M = 0.675$

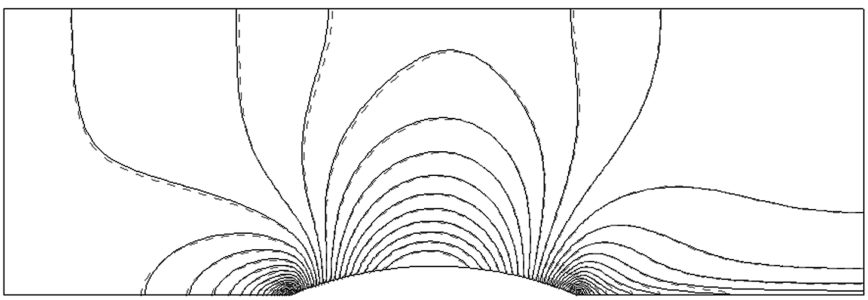

b) M=0.01

Fig. 23 Velocity magnitude for $Y_1 = 0.1$ mixture flow using AUSMPW+ (solid line) and RoeM (dashed line): a) $M = 0.675$ and b) $M = 0.01$.

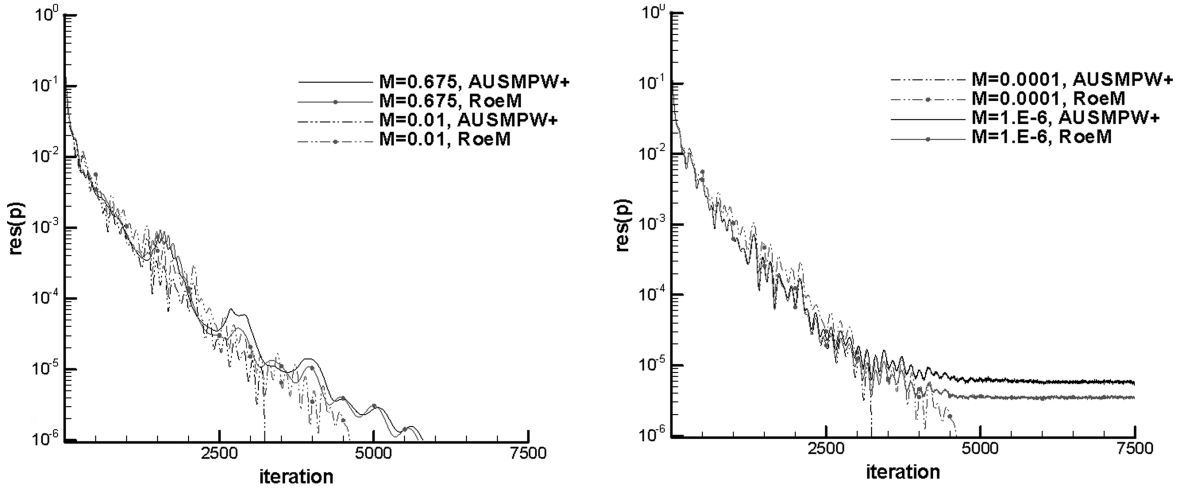

a) $M = 0.675, 0.01$ b) $M = 1\times10^{-4}, 1\times10^{-6}$

Fig. 24 Convergence history for $Y_1 = 0.1$ mixture bump flow: a) $M = 0.675$ and 0.01 and b) $M = 1 \times 10^{-4}$ and 1×10^{-6}.

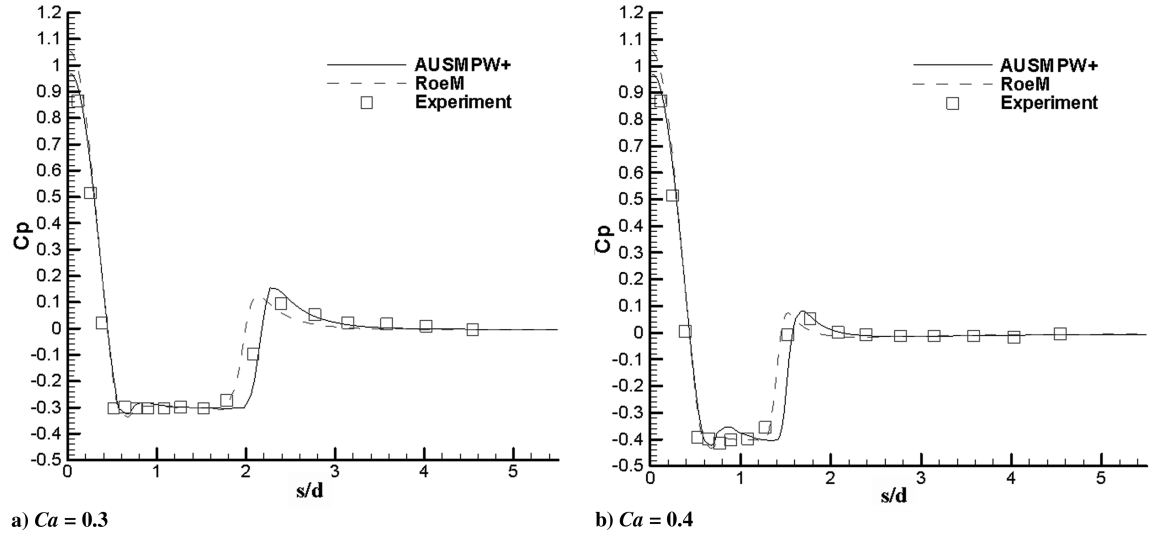

a) $Ca = 0.3$ b) $Ca = 0.4$

Fig. 25 Comparison of surface-pressure distribution with experimental data from [30]: a) $Ca = 0.3$ and b) $Ca = 0.4$.

compromising accuracy, efficiency, and robustness. A shock-discontinuity-sensing term (SDST), which plays a critical role in AUSMPW+ and RoeM, is newly derived from the mixture EOS, and its performance is analyzed for two-phase flows.

Three items are modified for the development of two-phase AUSMPW+ scheme. The first is to introduce a new SDST into the pressure-based weight functions ω and $f_{L,R}$. The numerical speed of sound at a cell interface is then modified by considering the physical situation of the phase-interfacial speed of sound in the HEM. Finally, the control function $f_{L,R}$ is scaled by reflecting the density difference across a cell interface for the treatment of a large-density-ratio phase interface. The two-phase RoeM scheme is derived from the two-phase Roe scheme by implementing the new SDST into the Mach-number-based weight functions f and g. The two-phase RoeM scheme is designed to maintain the merits of the original RoeM in gas dynamics: that is, the shock-stability, the total enthalpy conservation, and the numerical stability in the expansion region.

All-speed versions of the two-phase AUSMPW+ and RoeM are then obtained by employing the AUSM-type and HLLC-type preconditioning strategies. From the asymptotic analysis, it is observed that the discretized system by the preconditioned two-phase AUSMPW+ and RoeM schemes is consistent with the continuum system in the incompressible limit.

Numerical tests, from highly compressible to nearly incompressible flow conditions, are performed for various two-phase flows including large-density-ratio phase-interface problems. Comparisons confirm that the proposed schemes maintain shock-stable characteristics even in two-phase flows and describe two-phase wave physics based on the homogeneous-equilibrium model. In addition, the computed results involving low-Mach-number flows indicates that the preconditioned two-phase AUSMPW+ and RoeM are successfully working at all-speed flow regions.

Appendix: Incompressible-Limit Forms of Preconditioned Two-Phase AUSMPW+ and RoeM

I. Continuous Case: Conservations Laws for HEM Two-Phase Flows

We briefly examine the limits of the HEM compressible Euler equations as the Mach number goes to zero. Denoting the reference quantities with a subscript $*$, we select (L_*, U_*) to nondimensionalize $(t, \mathbf{x}, \mathbf{u})$ and (ρ_{m*}, c_*^2) to nondimensionalize (ρ_m, p, e_m). Then we obtain the system of nondimensionalized equations as follows. Here, $(\,)^l$ indicates a nondimensionalized quantity:

$$\frac{\partial \rho_m^l}{\partial t^l} + \nabla \cdot \rho_m^l \mathbf{u}^l = 0 \tag{A1a}$$

$$\frac{\partial \rho_m^l \mathbf{u}^l}{\partial t^l} + \nabla \cdot \rho_m^l \mathbf{u}^l \mathbf{u}^l + \frac{1}{M_*^2} \nabla p^l = 0 \tag{A1b}$$

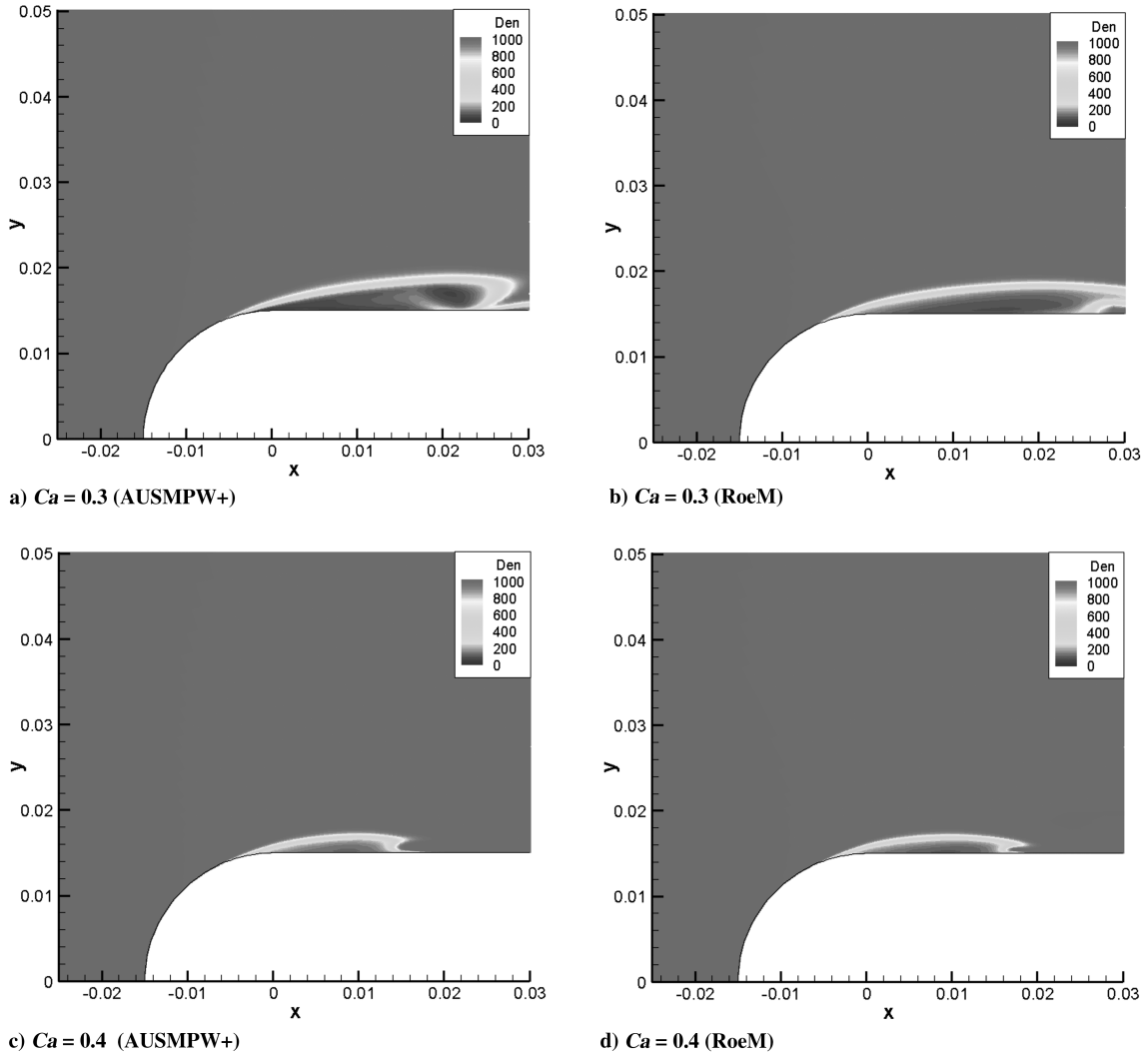

a) $Ca = 0.3$ (AUSMPW+) b) $Ca = 0.3$ (RoeM)

c) $Ca = 0.4$ (AUSMPW+) d) $Ca = 0.4$ (RoeM)

Fig. 26 Cavitation prediction for the density contour: a) $Ca = 0.3$ (AUSMPW+), b) $Ca = 0.3$ (RoeM), c) $Ca = 0.4$ (AUSMPW+), and d) $Ca = 0.4$ (RoeM).

$$\frac{\partial \rho_m^l E_t^l}{\partial t^l} + \nabla \cdot \rho_m^l H^l \mathbf{u}^l = 0 \tag{A1c}$$

$$\frac{\partial \rho_m^l Y_1}{\partial t^l} + \nabla \cdot \rho_m^l Y_1 \mathbf{u}^l = 0 \tag{A1d}$$

where $M_* = U_*/c_*$ is the reference Mach number. Using the relations $\rho_m^l Y_1 = \hat{\rho}_1^l \alpha_1$ and $\hat{\rho}_i^l = \text{const}$ in the incompressible limit, Eq. (A1d) is changed into the well-known volume-fraction transport equation for incompressible two-phase flows: $\partial \alpha_1/\partial t^l + \nabla \cdot \alpha_1 \mathbf{u}^l = 0$.

We introduce the following expansion in power of the Mach number in Eqs. (A1a–A1d):

$$\mathbf{q} = \mathbf{q}^{(0)} + M_* \mathbf{q}^{(1)} + M_*^2 \mathbf{q}^{(2)} + \cdots \tag{A2}$$

where $\mathbf{q} = [\rho_m^l, \mathbf{u}^l, E_t^l, Y_1]^T$. Collecting all the terms with the equal power of M_*, we obtain the following.

For $\mathcal{O}(1/M_*^2)$,

$$\nabla p^{l(0)} = 0 \tag{A3}$$

For $\mathcal{O}(1/M_*)$,

$$\nabla p^{l(1)} = 0 \tag{A4}$$

For $\mathcal{O}(1)$,

$$\frac{\partial \rho_m^{l(0)}}{\partial t^l} + \nabla \cdot \rho_m^{l(0)} \mathbf{u}^{l(0)} = 0 \tag{A5a}$$

$$\frac{\partial \rho_m^{l(0)} \mathbf{u}^{l(0)}}{\partial t^l} + \nabla \cdot \rho_m^{l(0)} \mathbf{u}^{l(0)} \mathbf{u}^{l(0)} + \frac{1}{M_*^2} \nabla p^{l(2)} = 0 \tag{A5b}$$

$$\frac{\partial \rho_m^{l(0)} E_t^{l(0)}}{\partial t^l} + \nabla \cdot (\rho_m^{l(0)} E_t^{l(0)} + p^{l(0)}) \mathbf{u}^{l(0)} = 0 \tag{A5c}$$

$$\frac{\partial \rho_m^{l(0)} Y_1^{(0)}}{\partial t^l} + \nabla \cdot \rho_m^{l(0)} Y_1^{(0)} \mathbf{u}^{l(0)} = 0 \tag{A5d}$$

From Eq. (A5b), the zeroth-order velocity is related to the second-order pressure, and thus the numerical dissipation with pressure difference should be scaled in a consistent manner. Regarding this, Liou [24] proposed the following lemma in the incompressible limit and proved it for the discrete system with the AUSM$^+$up scheme.

Lemma. The discrete system derived for $M_* \to 0$ is consistent to the order of Δx^l and dissipative approximation to the continuum system; that is,

$$\frac{\partial \rho^{l(0)}}{\partial t^l} + \nabla \cdot \rho^{l(0)} \mathbf{u}^{l(0)} = \frac{\partial}{\partial x_k^l}\left(\mu^l \frac{\partial p^{l(2)}}{\partial x_k^l}\right) \tag{A6a}$$

if the dissipation coefficient

$$\mu^l = \mathcal{O}(\Delta x^l) > 0 \tag{A6b}$$

and is independent of M_*. The dissipation is directly related to the spatial variation of the second-order pressure expansion $p^{l(2)}$.

II. Discrete Case 1: Preconditioned Two-Phase AUSMPW+ Scheme

The numerical flux of AUSM-type schemes can be divided with convective and pressure fluxes as

$$E_{1/2} = E_{1/2}^{(c)} + E_{1/2}^{(p)} \tag{A7}$$

The convective and the pressure fluxes of the two-phase AUSMPW+ scheme in Sec. V.A are

$$E_{1/2}^{(c)} = \bar{M}_L^+ c_{1/2} Q_L^* + \bar{M}_R^- c_{1/2} Q_R^* \tag{A8a}$$

$$E_{1/2}^{(p)} = P_L^+ P_L + P_R^- P_R \tag{A8b}$$

For $0 \le M_{1/2} \le 1$,

$$\bar{M}_L^+ = M_L^+ + M_R^-[(1-\omega)(1+f_R^*) - f_L^*] \tag{A9a}$$

$$\bar{M}_R^- = M_R^- \omega (1 + f_R^*) \tag{A9b}$$

With the relations $Q_R^* = Q_L^* + \Delta Q^*$ and $f_R^* = f_L^* + \Delta f^*$, the convective flux is written as

$$\begin{aligned} E_{1/2}^{(c)} &= c_{1/2}\{M_L^+ + M_R^-[(1-\omega)(1+f_R^*) - f_L^*]\}Q_L^* \\ &\quad + c_{1/2} M_R^- \omega (1+f_R^*) Q_R^* = c_{1/2}\{(M_L^+ + M_R^-)Q_L^* \\ &\quad + \omega M_R^- \Delta Q^*\} + c_{1/2} M_R^-\{(Q_L^* + \omega \Delta Q^*)\Delta f^* + \omega f_L^* \Delta Q^*\} \end{aligned} \tag{A10}$$

Using van Leer splitting, $M_{L,R}^{\pm} = \pm \frac{1}{4}(M_{L,R} \pm 1)^2$,

$$M_L^+ + M_R^- = \tfrac{1}{2}(M_L + M_R) + \mathcal{O}(M^2) \ge 0 \tag{A11a}$$

$$M_R^- = -\tfrac{1}{2}(\tfrac{1}{2} - M_R) + \mathcal{O}(M^2) \le 0 \tag{A11b}$$

Now let us consider the preconditioned version of the AUSMPW+ scheme in Sec. VI.A. The convective flux is

$$E_{1/2}^{(c)} = \bar{M}_L^{*+} c_{1/2}^* Q_L^* + \bar{M}_R^{*-} c_{1/2}^* Q_R^* \tag{A12}$$

The definitions of $\bar{M}_L^{*\pm}$, $M_{L,R}^{**}$, $c_{1/2}^*$, $\phi_{1/2}$, and the modified pressure-based weight function $f_{L,R}^{**}$ are given in Sec. VI.A.

With $M = M_* M^l$, $M_r = M_* M_r^l$, $\phi = M_* \phi^l$, and $c^* = c_* c^l \times M_* \phi^l = u_* c^l \phi^l$, the scaled Mach number is

$$M_{L,R}^{**} = \frac{M_L^l + M_R^l}{2\phi^l} + \mathcal{O}(M_*^2) \tag{A13}$$

Then the Mach number splitting functions are

$$M_L^{*+} + M_R^{*-} = \frac{M_L^l + M_R^l}{2\phi^l} + \mathcal{O}(M_*^2) \ge 0 \tag{A14a}$$

$$M_R^{*-} = -\frac{1}{2}\left(\frac{1}{2} - \frac{M_L^l + M_R^l}{2\phi^l}\right) + \mathcal{O}(M_*^2) \le 0 \tag{A14b}$$

ω is a nondimensional quantity, and

$$\begin{aligned} f_{L,R}^{**} &= \left(\frac{\bar{p}_{L,R}^l}{\bar{p}_s^l} - 1\right) \times (1-\omega) \times \frac{\min(\rho_{m,L}^l, \rho_{m,R}^l)}{\rho_{m,L}^l} \\ &\quad \times \frac{1}{M_*^2 M_r^{l2}} = f_{L,R}^{**l} / M_*^2 \end{aligned} \tag{A15}$$

To examine the incompressible-limit form of the preconditioned AUSMPW+ scheme, let us take $M_* \to 0$. Then the convective flux becomes

$$\begin{aligned} E_{1/2}^{(c)} &= u_* c_{1/2}^l \left\{\left(\frac{M_L^l + M_R^l}{2}\right) Q_L^* - \omega \frac{1}{4}\left(\phi^l - \left(M_L^l + M_R^l\right)\right)\Delta Q^*\right\} \\ &\quad - u_* c_{1/2}^l \frac{1}{4}\left(\phi^l - \left(M_L^l + M_R^l\right)\right)\left\{(Q_L^* + \omega \Delta Q^*)\frac{\Delta f^{**l}}{M_*^2}\right. \\ &\quad \left. + \omega \frac{f_L^{**l}}{M_*^2}\Delta Q^*\right\} \end{aligned} \tag{A16}$$

$$\phi^l - \left(M_L^l + M_R^l\right) > 0$$

Taking a similar procedure, the pressure flux in the incompressible limit becomes

$$E_{1/2}^{(p)} = \frac{p_L^l + p_R^l}{2M_*^2} = \frac{p_s^l}{M_*^2} \tag{A17}$$

As M_* goes to zero, $\Pi_{1/2}^* \to 1$ and $\omega \to 0$; thus, the nondimensionalized mass flux $(\rho_m u)_L^l$ is given by

$$\begin{aligned} (\rho_m u)_L^l &= \rho_{m,L}^l c_{1/2}^l \left[\frac{1}{2}\left(M_L^l + M_R^l\right) - \frac{1}{4}\left(\phi^l - \left(M_L^l + M_R^l\right)\right)\frac{\Delta f^{**l}}{M_*^2}\right] \\ &= \frac{\rho_{m,L}^l c_{1/2}^l \left(M_L^l + M_R^l\right)}{2} - \frac{\min\left(\rho_{m,L}^l, \rho_{m,R}^l\right) c_{1/2}^l K_1 \Delta p^l}{M_*^2} \end{aligned} \tag{A18}$$

where

$$K_1 = \frac{\phi^l - \left(M_L^l + M_R^l\right)}{4 p_s^l M_r^{l2}} \times \mathcal{O}(1) \tag{A19}$$

Then the resultant incompressible-limit form of the AUSMPW+ scheme can be expressed as

$$E_{1/2}^{(\rho_m)} = (\rho_{m*} u_*)(\rho_m u)_{L/R}^l \tag{A20a}$$

$$E_{1/2}^{(\rho_m u)} = (\rho_{m*} u_*^2)\left((\rho_m u)_{L/R}^l u_{L/R} + \frac{p_s^l}{M_*^2}\right) \tag{A20b}$$

$$E_{1/2}^{(\rho_m E_t)} = (\rho_{m*} u_* c_*^2)(\rho_m u)_{L/R}^l H_{L/R} \tag{A20c}$$

$$E_{1/2}^{(\rho_m Y_1)} = (\rho_{m*} u_*)(\rho_m u)_{L/R}^l Y_{1,L/R} \tag{A20d}$$

where $()_{L/R} = \begin{cases} ()_L, & M_{1/2} \ge 0 \\ ()_R, & M_{1/2} < 0 \end{cases}$.

After expanding the variables using Eq. (A2) and by applying the resultant fluxes to the one-dimensional semidiscretized form,

$$\Delta x \frac{\partial Q}{\partial t} + E_{1/2} - E_{-1/2} = 0 \tag{A21}$$

we obtain the following expressions for the terms of $\mathcal{O}(1/M_*^2)$.

Mixture mass conservation:

$$\min\left(\rho_{m,j}^{l(0)}, \rho_{m,j+1}^{l(0)}\right) c_{1/2}^{l(0)} K_{1,1/2}^{(0)} \Delta_{1/2} p^{l(0)} - \min\left(\rho_{m,j-1}^{l(0)}, \rho_{m,j}^{l(0)}\right) c_{-1/2}^{l(0)} K_{1,-1/2}^{(0)} \Delta_{-1/2} p^{l(0)} = 0 \tag{A22a}$$

Mixture momentum conservation:

$$\min\left(\rho_{m,j}^{l(0)}, \rho_{m,j+1}^{l(0)}\right) c_{1/2}^{l(0)} u_{j/j+1}^{l(0)} K_{1,1/2}^{(0)} \Delta_{1/2} p^{l(0)} - \min\left(\rho_{m,j-1}^{l(0)}, \rho_{m,j}^{l(0)}\right) c_{-1/2}^{l(0)} u_{j-1/j}^{l(0)} K_{1,-1/2}^{(0)} \Delta_{-1/2} p^{l(0)} - (\Delta_{1/2} p^{l(0)} + \Delta_{-1/2} p^{l(0)})/2 = 0 \tag{A22b}$$

Mass conservation for phase 1:

$$\min\left(\rho_{m,j}^{l(0)}, \rho_{m,j+1}^{l(0)}\right) c_{1/2}^{l(0)} Y_{1,j/j+1}^{(0)} K_{1,1/2}^{(0)} \Delta_{1/2} p^{l(0)} - \min\left(\rho_{m,j-1}^{l(0)}, \rho_{m,j}^{l(0)}\right) c_{-1/2}^{l(0)} Y_{1,j-1/j}^{(0)} K_{1,-1/2}^{(0)} \Delta_{-1/2} p^{l(0)} = 0 \tag{A22c}$$

where $(\,)_{j/j+1}$ is defined in the same manner as $(\,)_{L/R}$, and $\Delta_{1/2}(\,) = (\,)_{j+1} - (\,)_j$ and $\Delta_{-1/2}(\,) = (\,)_j - (\,)_{j-1}$. Note that the mixture density is a function of mass fraction only in the incompressible limit. To satisfy Eqs. (A22a–A22c) for an arbitrary velocity and mass-fraction field, $\Delta_{\pm 1/2} p^{l(0)} = 0$ for all j. Thus,

$$p_j^{l(0)} = p_j^{l(0)}(t) \quad \forall\ j \Leftrightarrow p_j^{l(0)} = \text{const in space} \tag{A23}$$

For the terms of $\mathcal{O}(1/M_*)$, by taking a similar procedure, we obtain

$$p_j^{l(1)} = p_j^{l(1)}(t) \quad \forall\ j \Leftrightarrow p_j^{l(1)} = \text{const in space} \tag{A24}$$

For the terms of $\mathcal{O}(1)$,
Mixture mass conservation:

$$\Delta x^l \frac{\partial \rho_{m,j}^{l(0)}}{\partial t^l} + \frac{1}{2}\left[\rho_{m,j/j+1}^{l(0)}\left(u_j^{l(0)} + u_{j+1}^{l(0)}\right) - \rho_{m,j-1/j}^{l(0)}\left(u_{j-1}^{l(0)} + u_j^{l(0)}\right)\right] - \left[\min\left(\rho_{m,j}^{l(0)}, \rho_{m,j+1}^{l(0)}\right) c_{1/2}^{l(0)} K_{1,1/2}^{(0)} \Delta_{1/2} p^{l(2)} - \min\left(\rho_{m,j-1}^{l(0)}, \rho_{m,j}^{l(0)}\right) c_{-1/2}^{l(0)} K_{1,-1/2}^{(0)} \Delta_{-1/2} p^{l(2)}\right] = 0 \tag{A25a}$$

Mass conservation for phase 1:

$$\Delta x^l \frac{\partial \rho_{m,j}^{l(0)} Y_{1,j}^{l(0)}}{\partial t^l} + \frac{1}{2}\left[\rho_{m,j/j+1}^{l(0)} Y_{1,j/j+1}^{(0)}\left(u_j^{l(0)} + u_{j+1}^{l(0)}\right) - \rho_{m,j-1/j}^{l(0)} Y_{1,j-1/j}^{(0)}\left(u_{j-1}^{l(0)} + u_j^{l(0)}\right)\right] - \left[\min\left(\rho_{m,j}^{l(0)}, \rho_{m,j+1}^{l(0)}\right) c_{1/2}^{l(0)} Y_{1,j/j+1}^{(0)} K_{1,1/2}^{(0)} \Delta_{1/2} p^{l(2)} - \min\left(\rho_{m,j-1}^{l(0)}, \rho_{m,j}^{l(0)}\right) c_{-1/2}^{l(0)} Y_{1,j-1/j}^{(0)} K_{1,-1/2}^{(0)} \Delta_{-1/2} p^{l(2)}\right] = 0 \tag{A25b}$$

By taking $\Delta x \to 0$, the limiting counterparts of Eqs. (A25a) and (A25b) are

$$\frac{\partial \rho_m^{l(0)}}{\partial t^l} + \frac{\partial \rho_m^{l(0)} u^{l(0)}}{\partial x^l} = \frac{\partial}{\partial x^l}\left(\mu^l \frac{\partial p^{l(2)}}{\partial x^l}\right) + \mathcal{O}(\Delta x^{l2}) \tag{A26a}$$

$$\frac{\partial \rho_m^{l(0)} Y_1^{(0)}}{\partial t^l} + \frac{\partial \rho_m^{l(0)} Y_1^{(0)} u^{l(0)}}{\partial x^l} = \frac{\partial}{\partial x^l}\left(\mu^l Y_1^{(0)} \frac{\partial p^{l(2)}}{\partial x^l}\right) + \mathcal{O}(\Delta x^{l2}) \tag{A26b}$$

with

$$\mu^l = \rho_m^{l(0)} c^{l(0)} K_1^{(0)} \Delta x^l > 0 \tag{A27}$$

All of the preceding results have shown that the discrete equations by the preconditioned two-phase AUSMPW+ are consistent with the continuum case, which satisfies the lemma in the incompressible limit.

III. Discrete Case 2: Preconditioned Two-Phase RoeM Scheme

The preconditioned two-phase RoeM scheme in Sec. VI.B has the following form:

$$E_{1/2} = \frac{1}{2}[E_L + E_R - \tilde{M}^* \Delta E + \hat{D}(\tilde{M}^{*2} - 1)\Delta Q^* + g\hat{D}(1 - |\tilde{M}^*|)B\Delta Q^{**}] \tag{A28}$$

where $\tilde{M}^* = \text{sign}(\hat{M}^*) \times \min(1, |\hat{M}^*|)$ and $\hat{M}^* = \hat{U}'/\hat{D}$. The detailed definitions are given in Secs. V.B and VI.B. Using the dimensionless quantities, $\hat{M}^* = \hat{M}^l/\hat{\phi}^l = \hat{M}^*$ and $\hat{D} = u_* \hat{D}^l$.

Let us take $M_* \to 0$ to examine the incompressible-limit form of Eq. (A28). Then $\Pi_{1/2}^* \to 1$, $f, g \to 1$, and the incompressible-limit form of the RoeM scheme is given by

$$E_{1/2}^{(\rho_m)} = \frac{1}{2}\rho_{m*} u_* \left[\{(1 + \hat{M}^*)\rho_{m,L}^l u_L^l + (1 - \hat{M}^*)\rho_{m,R}^l u_R^l\} + \hat{D}^l(\hat{M}^{*2} - 1)\Delta\rho_m^l + \hat{D}^l(1 - |\hat{M}^*|)\left(\Delta\rho_m^l - \frac{\Delta p^l}{\hat{D}^{l2} M_*^2}\right)\right] \tag{A29a}$$

$$E_{1/2}^{(\rho_m u)} = \frac{1}{2}\rho_{m*} u_*^2 \left[\left\{(1 + \hat{M}^*)\left(\rho_{m,L}^l u_L^{l2} + \frac{p_L^l}{M_*^2}\right) + (1 - \hat{M}^*)\left(\rho_{m,R}^l u_R^{l2} + \frac{p_R^l}{M_*^2}\right)\right\} + \hat{D}^l(\hat{M}^{*2} - 1)\Delta\rho_m^l u^l + \hat{D}^l(1 - |\hat{M}^*|)\hat{u}^l\left(\Delta\rho_m^l - \frac{\Delta p^l}{\hat{D}^{l2} M_*^2}\right)\right] \tag{A29b}$$

$$E_{1/2}^{(\rho_m Y_1)} = \frac{1}{2}\rho_{m*} u_* \left[\{\left(1 + \hat{M}^*\right)\rho_{m,L}^l u_L^l Y_{1,L} + (1 - \hat{M}^*)\rho_{m,R}^l u_R^l Y_{1,R}\right\} + \hat{D}^l(\hat{M}^{*2} - 1)\Delta\rho_m^l Y_1 + \hat{D}^l(1 - |\hat{M}^*|)\hat{Y}_1\left(\Delta\rho_m^l - \frac{\Delta p^l}{\hat{D}^{l2} M_*^2}\right)\right] \tag{A29c}$$

We note that for two-phase flow in the incompressible limit, the mixture density is the function of mass fraction only. Thus, we have the relations

$$\Delta\rho_m^l = \widehat{\frac{\partial \rho_m^l}{\partial Y_1}} \Delta Y_1$$

and

$$\Delta\rho_m^l Y_1 = \left(\hat{\rho}_m^l + \hat{Y}_1 \widehat{\frac{\partial \rho_m^l}{\partial Y_1}}\right)\Delta Y_1$$

Then Eqs. (A29a) and (A29c) can be rearranged as follows:

$$E_{1/2}^{(\rho_m)} = \frac{1}{2}\rho_{m*} u_* \left[\left\{(1 + \hat{M}^*)\rho_{m,L}^l u_L^l + (1 - \hat{M}^*)\rho_{m,R}^l u_R^l\right\} - \frac{1 - |\hat{M}^*|}{\hat{D}^l}\frac{\Delta p^l}{M_*^2} - \hat{D}^l(|\hat{M}^*| - \hat{M}^{*2})\widehat{\frac{\partial \rho_m^l}{\partial Y_1}}\Delta Y_1\right] \tag{A30a}$$

$$E_{1/2}^{(\rho_m Y_1)} = \frac{1}{2}\rho_{m*}u_*\left[\left\{(1+\hat{M}^*)\rho_{m,L}^l u_L^l Y_{1,L} + (1-\hat{M}^*)\rho_{m,R}^l u_R^l Y_{1,R}\right\} - \frac{(1-|\hat{M}^*|)\hat{Y}_1}{\hat{D}^l}\frac{\Delta p^l}{M_*^2} - \hat{D}^l\left\{(1-\hat{M}^{*2})\hat{\rho}_m^l + (|\hat{M}^*| - \hat{M}^{*2})\hat{Y}_1\widehat{\frac{\partial\rho_m^l}{\partial Y_1}}\right\}\Delta Y_1\right] \quad \text{(A30b)}$$

where $\hat{D}^l > 0$, $1-|\hat{M}^*| > 0$, $|\hat{M}^*| - \hat{M}^{*2} > 0$, and $1-\hat{M}^{*2} > 0$.

After expanding the variables using Eq. (A2) and by applying the fluxes to the one-dimensional semidiscretized form of Eq. (A21), we obtain the following results for the terms of $\mathcal{O}(1/M_*^2)$.

Mixture mass conservation:

$$\frac{1-|\hat{M}_{1/2}^{*(0)}|}{\hat{D}_{1/2}^{l(0)}}\Delta_{1/2}p^{l(0)} - \frac{1-|\hat{M}_{-1/2}^{*(0)}|}{\hat{D}_{-1/2}^{l(0)}}\Delta_{-1/2}p^{l(0)} = 0 \quad \text{(A31a)}$$

Mixture momentum conservation:

$$\frac{\left(1-|\hat{M}_{1/2}^{*(0)}|\right)\hat{u}_{1/2}^{l(0)}}{\hat{D}_{1/2}^{l(0)}}\Delta_{1/2}p^{l(0)} - \frac{\left(1-|\hat{M}_{-1/2}^{*(0)}|\right)\hat{u}_{-1/2}^{l(0)}}{\hat{D}_{-1/2}^{l(0)}}\Delta_{-1/2}p^{l(0)} + \left\{\left(1-\hat{M}_{1/2}^{*(0)}\right)\Delta_{1/2}p^{l(0)} + \left(1+\hat{M}_{-1/2}^{*(0)}\right)\Delta_{-1/2}p^{l(0)}\right\} = 0 \quad \text{(A31b)}$$

Mass conservation for phase 1:

$$\frac{\left(1-|\hat{M}_{1/2}^{*(0)}|\right)\hat{Y}_{1,1/2}^{(0)}}{\hat{D}_{1/2}^{l(0)}}\Delta_{1/2}p^{l(0)} - \frac{\left(1-|\hat{M}_{1/2}^{*(0)}|\right)\hat{Y}_{1,-1/2}^{(0)}}{\hat{D}_{-1/2}^{l(0)}}\Delta_{-1/2}p^{l(0)} = 0 \quad \text{(A31c)}$$

To satisfy Eqs. (A31a–A31c) for an arbitrary velocity and mass-fraction field, $\Delta_{\pm 1/2}p^{l(0)} = 0$ for all j. Thus,

$$p_j^{l(0)} = p_j^{l(0)}(t) \quad \forall\ j \Leftrightarrow p_j^{l(0)} = \text{const in space} \quad \text{(A32)}$$

For the terms of $\mathcal{O}(1/M_*)$, by taking a similar procedure, we obtain

$$p_j^{l(1)} = p_j^{l(1)}(t) \quad \forall\ j \Leftrightarrow p_j^{l(1)} = \text{const in space} \quad \text{(A33)}$$

For the terms of $\mathcal{O}(1)$,

Mixture mass conservation:

$$\Delta x^l\frac{\partial\rho_{m,j}^{l(0)}}{\partial t^l} + \frac{1}{2}\left[\left(1-\hat{M}_{1/2}^{*(0)}\right)\Delta_{1/2}\rho_m^{l(0)}u^{l(0)} + \left(1+\hat{M}_{-1/2}^{*(0)}\right)\Delta_{-1/2}\rho_m^{l(0)}u^{l(0)}\right] - \frac{1}{2}\left[\frac{1-|\hat{M}_{1/2}^{*(0)}|}{\hat{D}_{1/2}^{l(0)}}\Delta_{1/2}p^{l(2)} - \frac{1-|\hat{M}_{-1/2}^{*(0)}|}{\hat{D}_{-1/2}^{l(0)}}\Delta_{-1/2}p^{l(2)}\right] - \frac{1}{2}\left[\hat{D}_{1/2}^{l(0)}\left(|\hat{M}_{1/2}^{*(0)}| - \hat{M}_{1/2}^{*(0)2}\right)\widehat{\frac{\partial\rho_m^l}{\partial Y_1}}\Big|_{1/2}^{(0)}\Delta_{1/2}Y_1^{(0)} - \hat{D}_{-1/2}^{l(0)}\left(|\hat{M}_{-1/2}^{*(0)}| - \hat{M}_{-1/2}^{*(0)2}\right)\widehat{\frac{\partial\rho_m^l}{\partial Y_1}}\Big|_{-1/2}^{(0)}\Delta_{-1/2}Y_1^{(0)}\right] = 0 \quad \text{(A34a)}$$

Mass conservation for phase 1:

$$\Delta x^l\frac{\partial\rho_{m,j}^{l(0)}Y_1^{(0)}}{\partial t^l} + \frac{1}{2}\left[\left(1-\hat{M}_{1/2}^{*(0)}\right)\Delta_{1/2}\rho_m^{l(0)}u^{l(0)}Y_1^{(0)} + \left(1+\hat{M}_{-1/2}^{*(0)}\right)\Delta_{-1/2}\rho_m^{l(0)}u^{l(0)}Y_1^{(0)}\right] - \frac{1}{2}\left[\frac{\left(1-|\hat{M}_{1/2}^{*(0)}|\right)\hat{Y}_{1,1/2}^{(0)}}{\hat{D}_{1/2}^{l(0)}}\Delta_{1/2}p^{l(2)} - \frac{\left(1-|\hat{M}_{-1/2}^{*(0)}|\right)\hat{Y}_{1,-1/2}^{(0)}}{\hat{D}_{-1/2}^{l(0)}}\Delta_{-1/2}p^{l(2)}\right] - \frac{1}{2}\left[\hat{D}_{1/2}^{l(0)}\left\{\left(1-\hat{M}_{1/2}^{*(0)2}\right)\hat{\rho}_{m,1/2}^{l(0)} + \left(|\hat{M}_{1/2}^{*(0)}| - \hat{M}_{1/2}^{*(0)2}\right)\hat{Y}_{1,1/2}^{(0)}\widehat{\frac{\partial\rho_m^l}{\partial Y_1}}\Big|_{1/2}^{(0)}\right\}\Delta_{1/2}Y_1^{(0)} - \hat{D}_{1/2}^{l(0)}\left\{\left(1-\hat{M}_{-1/2}^{*(0)2}\right)\hat{\rho}_{m,-1/2}^{l(0)} + \left(|\hat{M}_{-1/2}^{*(0)}| - \hat{M}_{-1/2}^{*(0)2}\right)\hat{Y}_{1,-1/2}^{(0)}\widehat{\frac{\partial\rho_m^l}{\partial Y_1}}\Big|_{-1/2}^{(0)}\right\}\Delta_{-1/2}Y_1^{(0)}\right] = 0 \quad \text{(A34b)}$$

Again, by taking $\Delta x \to 0$, the limiting counterparts of Eqs. (A34a) and (A34b) are

$$\frac{\partial\rho_m^{l(0)}}{\partial t^l} + \frac{\partial\rho_m^{l(0)}u^{l(0)}}{\partial x^l} = \frac{\partial}{\partial x^l}\left(\mu_p^l\frac{\partial p^{l(2)}}{\partial x^l}\right) + \frac{\partial}{\partial x^l}\left(\mu_{Y_1}^l\frac{\partial Y_1^{l(0)}}{\partial x^l}\right) + O(\Delta x^{l2}) \quad \text{(A35a)}$$

$$\frac{\partial\rho_m^{l(0)}Y_1^{(0)}}{\partial t^l} + \frac{\partial\rho_m^{l(0)}Y_1^{(0)}u^{l(0)}}{\partial x^l} = \frac{\partial}{\partial x^l}\left(\mu_p^l Y_1^{(0)}\frac{\partial p^{l(2)}}{\partial x^l}\right) + \frac{\partial}{\partial x^l}\left(\mu_{Y_1Y_1}^l\frac{\partial Y_1^{l(0)}}{\partial x^l}\right) + O(\Delta x^{l2}) \quad \text{(A35b)}$$

with

$$\mu_p^l = \frac{1-|M^{*(0)}|}{D^{l(0)}}\Delta x^l > 0 \quad \text{(A36a)}$$

$$\mu_{Y_1}^l = D^{l(0)}(|M^{*(0)}| - M^{*(0)2})\left.\frac{\partial\rho_m^l}{\partial Y_1}\right|^{(0)}\Delta x^l > 0 \quad \text{(A36b)}$$

$$\mu_{Y_1Y_1}^l = D^{l(0)}(1-M^{*(0)2})\rho_m^{l(0)}\Delta x^l + Y_1^{(0)}\mu_{Y_1}^l > 0 \quad \text{(A36c)}$$

All of the preceding results have shown that the discrete equations by the preconditioned two-phase RoeM are consistent with the continuum case, which satisfies the lemma of Liou [24] in the incompressible limit. Moreover, it is observed that the discrete equations by RoeM have additional diffusion terms by mass-fraction difference, whereas the discrete equations by AUSMPW+ do not. However, a similar diffusion term can be produced in AUSMPW+ if the function ω is designed to work on a phase interface.

Acknowledgments

The authors appreciate the financial support by the Agency for Defense Development (ADD) and by the Brain Korea-21 Program for Mechanical and Aerospace Engineering Research at Seoul National University. The authors thank Kyu-Hong Kim for valuable discussion in preparing the earlier version of the present paper. The

authors also thank the reviewers for useful suggestions and valuable comments.

References

[1] Saurel, R., and Abgrall, R., "A Multiphase Godunov Method for Compressible Multifluid and Multiphase Flows," *Journal of Computational Physics*, Vol. 150, No. 2, 1999, pp. 425–467. doi:10.1006/jcph.1999.6187

[2] Städtke, H., *Gasdynamic Aspects of Two-Phase Flow*, Wiley-VCH Verlag, Weinheim, Germany, 2006.

[3] Kunz, R. F., Lindau, J. W., Billet, M. L., and Stinebring, D. R., "Multiphase CFD Modeling of Developed and Supercavitating Flows," *Supercavitating Flows*, NATO, Neuilly-sur-Seine, France, Feb. 2001.

[4] Owis, F. M., and Nayfeh, A. H., "Computations of the Compressible Multiphase Flow Over the Cavitating High-Speed Torpedo," *Journal of Fluids Engineering*, Vol. 125, No. 3, 2003, pp. 459–468. doi:10.1115/1.1568358

[5] Edwards, J. R., Franklin, R. K., and Liou, M.-S., "Low-Diffusion Flux-Splitting Methods for Real Fluid Flows with Phase Transitions," *AIAA Journal*, Vol. 38, No. 9, 2000, pp. 1624–1633. doi:10.2514/2.1145

[6] Neaves, M. D., and Edwards, J. R., "All-Speed Time-Accurate Underwater Projectile Calculations Using a Preconditioning Algorithm," *Journal of Fluids Engineering*, Vol. 128, No. 2, 2006, pp. 284–296. doi:10.1115/1.2169816

[7] Abgrall, R., and Karni, S., "Computations of Compressible Multifluids," *Journal of Computational Physics*, Vol. 169, No. 2, 2001, pp. 594–623. doi:10.1006/jcph.2000.6685

[8] Hankin, R. K. S., "The Euler Equations for Multiphase Compressible Flow in Conservation Form," *Journal of Computational Physics*, Vol. 172, No. 2, 2001, pp. 808–826. doi:10.1006/jcph.2001.6859

[9] Venkateswaran, S., and Merkle, C. L., "Analysis of Preconditioning Methods for the Euler and Navier-Stokes Equations," VKI Lecture Series 1999–03, Von Karman Inst. for Fluid Dynamics, Rhode-Saint-Genèse, Belgium, Mar. 1999.

[10] Turkel, E., "A Review of Preconditioning Methods for Fluid Dynamics," *Applied Numerical Mathematics*, Vol. 12, Nos. 1–3, 1993, pp. 257–284. doi:10.1016/0168-9274(93)90122-8

[11] Kim, K. H., Kim, C., and Rho, O. H., "Methods for the Accurate Computations of Hypersonic Flows, Part 1: AUSMPW+ Scheme," *Journal of Computational Physics*, Vol. 174, No. 1, 2001, pp. 38–80. doi:10.1006/jcph.2001.6873

[12] Kim, S. S., Kim, C., Rho, O. H., Hong, S. K., "Cures for the Shock Instability: Development of a Shock-Stable Roe Scheme," *Journal of Computational Physics*, Vol. 185, No. 2, 2003, pp. 342–374. doi:10.1016/S0021-9991(02)00037-2

[13] Kim, K. H., Lee, J. H., and Rho, O. H., "An Improvement of AUSM Schemes by Introducing the Pressure-Based Weight Functions," *Computers and Fluids*, Vol. 27, No. 3, 1998, pp. 311–346. doi:10.1016/S0045-7930(97)00069-8

[14] Edwards, J. R., and Liou, M.-S., "Low-Diffusion Flux-Splitting Methods for Flows at All Speeds," *AIAA Journal*, Vol. 36, No. 9, 1998, pp. 1610–1617. doi:10.2514/2.587

[15] Luo, H., Baum, J. D., and Löhner, R., "Extension of Harten-Lax-van Leer Scheme for Flows at All Speeds," *AIAA Journal*, Vol. 43, No. 6, 2005, pp. 1160–1166. doi:10.2514/1.7567

[16] Li, D., Sankaran, V., Lindau, J. W., and Merkle, C. L., "Computational Formulation for Multi-Phase and Multi-Component Flows," 43rd AIAA Aerospace Sciences Meeting and Exhibit, AIAA Paper 2005-1391, Reno, NV, 2005.

[17] Luo, H., Baum, J. D., and Löhner, R., "On the Computation of Multimaterial Flows Using ALE Formulation," *Journal of Computational Physics*, Vol. 194, No. 1, 2004, pp. 304–328. doi:10.1016/j.jcp.2003.09.026

[18] Kitamura, K., Roe, R., and Farzad, I., "An Evaluation of Euler Fluxes for Hypersonic Flow Computations," 18th AIAA Computational Fluid Dynamics Conference, AIAA Paper 2007-4465, June 2007.

[19] Liu, T. G., Khoo, B. C., and Yeo, K. S., "The Simulation of Compressible Multimedium Flow 2: Application to 2D Underwater Shock Refraction," *Computers and Fluids*, Vol. 30, No. 3, 2001, pp. 315–337. doi:10.1016/S0045-7930(00)00021-9

[20] Peng, D.-Y., and Robinson, D. B., "A New Two-Constant Equation of State," *Industrial and Engineering Chemistry Fundamentals*, Vol. 15, No. 1, 1976, pp. 59–64. doi:10.1021/i160057a011

[21] Chang, M.-Y., and Morsi, B. I., "Mass Transfer Characteristics of Gases in Aqueous and Organic Liquids at Elevated Pressure and Temperatures in Agitated Reactors," *Chemical Engineering Science*, Vol. 46, No. 10, 1991, pp. 2639–2650. doi:10.1016/0009-2509(91)80057-6

[22] Kim, K. H., and Kim, C., "Accurate, Efficient And Monotonic Numerical Methods for Multidimensional Compressible Flows, Part 1: Spatial Discretization," *Journal of Computational Physics*, Vol. 208, No. 2, 2005, pp. 527–569. doi:10.1016/j.jcp.2005.02.021

[23] Guillard, H., and Viozat, C., "On the Behaviour of Upwind Schemes in the Low Mach Number Limit," *Computers and Fluids*, Vol. 28, No. 1, 1999, pp. 63–86. doi:10.1016/S0045-7930(98)00017-6

[24] Liou, M.-S., "A Sequel to AUSM, Part 2: AUSM+up for All Speeds," *Journal of Computational Physics*, Vol. 214, No. 1, 2006, pp. 137–170. doi:10.1016/j.jcp.2005.09.020

[25] Gottlieb, S., and Shu, C. W., "Total Variation Diminishing Runge-Kutta Schemes," *Mathematics of Computation*, Vol. 67, No. 221, 1998, pp. 73–85. doi:10.1090/S0025-5718-98-00913-2

[26] Sanders, R., Morano, E., and Druguet, M.-C., "Multidimensional Dissipation for Upwind Schemes: Stability and Applications to Gas Dynamics," *Journal of Computational Physics*, Vol. 145, No. 2, 1998, pp. 511–537. doi:10.1006/jcph.1998.6047

[27] Kim, K. H., and Kim, C."Accurate, Efficient and Monotonic Numerical Methods for Multidimensional Compressible Flows Part 2: Multi-Dimensional Limiting Process," *Journal of Computational Physics*, Vol. 208, No. 2, 2005, pp. 570–615. doi:10.1016/j.jcp.2005.02.022

[28] Ballhaus, W. F., Jr., and Holt, M., "Interaction Between the Ocean Surface and Underwater Spherical Blast Waves," *Physics of Fluids*, Vol. 17, No. 6, 1974, pp. 1068–1079. doi:10.1063/1.1694845

[29] Merkle, C. L., Feng, J., and Buelow, P. E. O., "Computational Modeling of the Dynamics of Sheet Cavitation," *Third International Symposium on Cavitation*, Vol. 2, Univ. Joseph Fourier, Grenoble, France, 1998, pp. 307–311.

[30] Rouse, H., and McNown, J. S., "Cavitation and Pressure Distribution, Head Forms at Zero Angle of Yaw," *Studies in Engineering*, Bulletin 32, State Univ. of Iowa, Iowa City, IA, 1948.

Z. Wang
Associate Editor